

# Polynomial reconstruction of the magnetic field observed by multiple spacecraft with integrated velocity determination

Richard E. Denton<sup>1</sup>, Yi-Hsin Liu<sup>1</sup>, Hiroshi Hasegawa<sup>2</sup>, Roy B. Torbert<sup>3</sup>, Wenya Li<sup>4</sup>, Stephen A. Fuselier<sup>5</sup>, and James L Burch<sup>5</sup>

<sup>1</sup>Dartmouth College

<sup>2</sup>Institute of Space and Astronautical Science, JAXA

<sup>3</sup>University of New Hampshire

<sup>4</sup>National Space Science Center, Chinese Academy of Sciences

<sup>5</sup>Southwest Research Institute

November 24, 2022

## Abstract

Recently a polynomial reconstruction technique has been developed for reconstructing the magnetic field in the vicinity of multiple spacecraft, and has been applied to events observed by the Magnetospheric Multiscale (MMS) mission. Whereas previously the magnetic field was reconstructed using spacecraft data from a single time, here we extend the method to allow input over a span of time. This extension increases the amount of input data to the model, improving the reconstruction results, and allows the velocity of the magnetic structure to be calculated. The effect of this modification, as well as many other options, is explored by comparing reconstructed fields to those of a three-dimensional particle in cell simulation of magnetic reconnection, using virtual spacecraft data as input. We often find best results using multiple-time input, a moderate amount of smoothing of the input data, and a model with a reduced set of parameters based on the ordering that the maximum, intermediate, and minimum values of the gradient of the vector magnetic field are well separated. When spacecraft input data are temporally smoothed, reconstructions are representative of spatially smoothed fields. Two MMS events are reconstructed. The first of these was late in the mission when it was not possible to use the current density for MMS4 because of its instrument failure. The second shows a rotational discontinuity without an X or O line. In both cases, the reconstructions yield a visual representation of the magnetic structure that is consistent with earlier studies.

1                   **Polynomial reconstruction of the magnetic field**  
2                   **observed by multiple spacecraft with integrated**  
3                   **velocity determination**

4                   **Richard E. Denton<sup>1</sup>, Yi-Hsin Liu<sup>1</sup>, Hiroshi Hasegawa<sup>2</sup>, Roy B. Torbert<sup>3</sup>,**  
5                   **Wenya Li<sup>4</sup>, Stephen Fuselier<sup>5,6</sup>, and James L. Burch<sup>5</sup>**

6                   <sup>1</sup>Department of Physics and Astronomy, Dartmouth College, Hanover, New Hampshire, USA

7                   <sup>2</sup>Institute of Space and Astronautical Science, JAXA, Sagami-hara, Japan

8                   <sup>3</sup>Institute for the Study of Earth, Oceans, and Space, University of New Hampshire, Durham, New  
9                   Hampshire, USA

10                  <sup>4</sup>State Key Laboratory of Space Weather, National Space Science Center, Chinese Academy of Sciences,  
11                  Beijing, China

12                  <sup>5</sup>Space Science and Engineering Division Southwest Research Institute, San Antonio, Texas, USA

13                  <sup>6</sup>University of Texas at San Antonio, San Antonio, Texas, USA

14                  **Key Points:**

- 15                  • Polynomial reconstruction using multiple input times yields improved reconstruc-  
16                  tions and an estimate of the structure velocity.
- 17                  • Using reconstructions of simulation data, the effect of various options is explored  
18                  and recommendations for method are made.
- 19                  • Two MMS events are reconstructed, showing that events lacking MMS4 current  
20                  density and events without an X line are also reconstructed.

---

Corresponding author: Richard E. Denton, redenton at gmail dot com

**Abstract**

Recently a polynomial reconstruction technique has been developed for reconstructing the magnetic field in the vicinity of multiple spacecraft, and has been applied to events observed by the Magnetospheric Multiscale (MMS) mission. Whereas previously the magnetic field was reconstructed using spacecraft data from a single time, here we extend the method to allow input over a span of time. This extension increases the amount of input data to the model, improving the reconstruction results, and allows the velocity of the magnetic structure to be calculated. The effect of this modification, as well as many other options, is explored by comparing reconstructed fields to those of a three-dimensional particle in cell simulation of magnetic reconnection, using virtual spacecraft data as input. We often find best results using multiple-time input, a moderate amount of smoothing of the input data, and a model with a reduced set of parameters based on the ordering that the maximum, intermediate, and minimum values of the gradient of the vector magnetic field are well separated. When spacecraft input data are temporally smoothed, reconstructions are representative of spatially smoothed fields. Two MMS events are reconstructed. The first of these was late in the mission when it was not possible to use the current density for MMS4 because of its instrument failure. The second shows a rotational discontinuity without an X or O line. In both cases, the reconstructions yield a visual representation of the magnetic structure that is consistent with earlier studies.

**Plain Language Summary**

The magnetic field plays a crucial role in many space physics processes. Ideally, we would image the magnetic field, but spacecraft make only point observations. Reconstruction techniques allow us to infer the structure of the magnetic field around the trajectory of spacecraft and to visualize that structure. Here we extend our previous technique of polynomial expansion of the magnetic field by using input from spacecraft over a span of time rather than at just one point in time. We test the new technique, as well as our previous technique, by reconstructing the magnetic field around the trajectory of virtual spacecraft flying through a simulation of magnetic reconnection. Then we use our new technique to reconstruct the magnetic field around the trajectory of the Magnetospheric Multiscale (MMS) spacecraft for two events observed in space.

**1 Introduction**

The magnetic field plays a crucial role in magnetic reconnection and other space physics processes. In order to understand these processes, it is helpful to determine the structure of the magnetic field and the velocity of that structure relative to the spacecraft. Single spacecraft techniques to determine both the structure and velocity include reconstruction based on Grad-Shafranov equilibrium (Sonnerup et al., 2006, and references therein), magnetohydrodynamics (MHD) and Hall MHD (Sonnerup & Teh, 2008, 2009), and electron MHD (EMHD) (Hasegawa et al., 2019; Korovinskiy et al., 2021, and references therein). Empirical models using observations by multiple spacecraft of the magnetic field have also been developed. First order Taylor expansion (FOTE) of the magnetic field has been described by Fu et al. (2015, 2016, 2020). Recently Torbert et al. (2020) and then Denton et al. (2020) extended this technique to a quadratic model using the current density measured by the spacecraft as an input to the model, and applied these techniques to events observed by the Magnetospheric Multiscale (MMS) mission. The empirical methods have fewer assumptions than the single spacecraft techniques and yield time-dependent maps of the magnetic field around the spacecraft.

Using the reconstruction method of Denton et al. (2020), Denton et al. (2021) used the varying location of the reconstructed reconnection X-line relative to the spacecraft to estimate the velocity of the magnetic structure. (The reconnection X-line is the magnetic null of the magnetic field in the plane containing the reconnection magnetic field

and direction across the current sheet.) Basically, this technique assumed that the reconnection structure, or at least the position of the X-line, was time stationary or at least slowly varying. In this paper, we will also use polynomial reconstruction to reconstruct the magnetic field and determine the structure velocity, but using a more integrated technique. We will assume that the structure velocity is constant during some segment of time that includes multiple times at which the data was sampled, and will find the velocity and reconstruction parameters that lead to a best fit to all the spacecraft magnetic field and current density observations during that time segment. The resulting velocity optimizes the fit to all the data, not just the position of an inferred X-line. We will call this new method “multiple-time input”, as distinguished from the “single-time input” method of Denton et al. (2020).

Here we test the multiple-time input technique using data from a 3D particle-in-cell simulation of magnetic reconnection with small but nontrivial spatial variation out of the reconnection plane (Liu et al., 2019). Then we use this technique to determine the magnetic structure for two events observed by MMS.

In section 2 we briefly discuss the data and method, in section 3 we reconstruct the magnetic field for the simulation data, in section 4 we reconstruct the magnetic field for two MMS events. Finally in section 5 we summarize our results.

The largest section of this paper tests various options for reconstruction in section 3. For someone interested only in actual MMS events, they may want to skim through section 2 and then skip to section 4. Section 3 is important for learning what options work best and how well the reconstructions agree with the actual fields that are being reconstructed, but the results of section 3 are also summarized in section 5.

A new and key feature of our simulation data is that they are three dimensional. As we will see, it is challenging to accurately reconstruct the variation of the fields in the direction of least spatial variation (minimum gradient).

## 2 Reconstruction method

What we want to do is to get a quadratic expansion of the magnetic field in terms of the reconnection coordinates  $L$ ,  $M$ , and  $N$ ;  $L$  and  $N$  define the reconnection plane, where  $L$  is aligned with the direction of the reconnection magnetic field and  $N$  is the “normal” direction across the current sheet;  $M$  completes the coordinate system, and is ideally the direction of invariance, although that may not be the case if the  $L$  direction is determined based on maximum variance of  $\mathbf{B}$  (Denton et al., 2016, 2018). Note that we use  $L$ ,  $M$ , and  $N$  (or  $l$ ,  $m$ , and  $n$  discussed below) as either coordinates or component labels, similar to the way  $x$ ,  $y$ , and  $z$  are commonly used.

The complete quadratic expansion in terms of these coordinates is

$$\begin{aligned}
 B_i = & B_{i,0} + \frac{\partial B_i}{\partial L}L + \frac{\partial B_i}{\partial M}M + \frac{\partial B_i}{\partial N}N \\
 & + \frac{\partial^2 B_i}{\partial L^2} \frac{L^2}{2} + \frac{\partial^2 B_i}{\partial M^2} \frac{M^2}{2} + \frac{\partial^2 B_i}{\partial N^2} \frac{N^2}{2} \\
 & + \frac{\partial^2 B_i}{\partial L \partial M} LM + \frac{\partial^2 B_i}{\partial L \partial N} LN + \frac{\partial^2 B_i}{\partial M \partial N} MN,
 \end{aligned} \tag{1}$$

where the  $i$  subscript in  $B_i$  stands for  $L$ ,  $M$ , or  $N$ . The equations for  $\mu_0 \mathbf{J} = \nabla \times \mathbf{B}$  (neglecting the displacement current) and  $\nabla \cdot \mathbf{B} = \mathbf{0}$  are found by taking the curl or divergence of equations (1) as described in Appendix A. We assume that there are four spacecraft. And for each of these spacecraft, there are three components of  $\mathbf{B}$  and three components of  $\mathbf{J}$ , leading to 24 equations. There are also four equations from  $\nabla \cdot \mathbf{B} = \mathbf{0}$ , one for spatially constant terms, and three derived from terms proportional to  $L$ ,  $M$ , or  $N$  (Appendix A). For more details, see work by Denton et al. (2020).

114 For each of equations (1), with  $i = L, M,$  or  $N,$  there are 10 parameters; so al-  
 115 together, there are 30 parameters to determine at any one time. Using data from a sin-  
 116 gular time, there are 24 plus 4 equals 28 equations, not enough to solve for all 30 param-  
 117 eters. To get around this problem, Torbert et al. (2020) and Denton et al. (2020) used  
 118 models depending on the coordinates  $n, l,$  and  $m$  based on Minimum Directional Deriva-  
 119 tive (MDD) analysis, which calculates the gradient of the vector magnetic field measured  
 120 by four spacecraft (Shi et al., 2005, 2019);  $n, l,$  and  $m$  are the maximum, intermediate,  
 121 and minimum gradient eigenvector coordinates, respectively. Normally the direction of  
 122 the maximum gradient will be the direction across the current sheet,  $\sim \mathbf{e}_N$  (Denton et  
 123 al., 2018). Then if the minimum gradient is relatively steady and approximately in the  
 124  $\mathbf{e}_M$  direction,  $l, m,$  and  $n$  will be similar to  $L, M,$  and  $N.$

125 Based on the fact that the linear  $m$  dependence is by definition smallest, Torbert  
 126 et al. (2020) dropped the  $\partial^2 B_i / \partial m^2$  terms and used a superposition of solutions with  
 127 28 parameters in order to exactly match the values of  $\mathbf{B}$  and  $\mathbf{J}$  at the spacecraft posi-  
 128 tions. But Denton et al. (2020) showed that that procedure results in overfitting, lead-  
 129 ing to a solution that could wildly vary away from the spacecraft positions. The prob-  
 130 lem is similar to that resulting from use of a high order polynomial with respect to one  
 131 variable to exactly fit a number of data points. In order to avoid overfitting, Denton et  
 132 al. (2020) used a reduced set of terms based on the ordering  $\partial / \partial n \gg \partial / \partial l \gg \partial / \partial m.$

133 Now we introduce our multiple-time input approach using measurements over an  
 134 interval of time. We will assume that the spacecraft are moving through the magnetic  
 135 structure with a constant velocity for several observation times. This is similar in prin-  
 136 ciple to the method of Manuzzo et al. (2019), who used several data points to evaluate  
 137 the structure velocity from the potentially single-point Spatial-Temporal Difference (STD)  
 138 method of Shi et al. (2006). STD as implemented by Shi et al. (2006) assumes that the  
 139 time dependence of the magnetic field observed by all four spacecraft is due to convec-  
 140 tion through a steady spatial structure, and solves for the structure velocity from the  
 141 convection equation using the spatial gradient of the magnetic field evaluated at one time.  
 142 Most other systems of reconstruction also assume a constant velocity over a period of  
 143 time (e.g. Hasegawa et al., 2019).

144 Expanding  $L, M,$  and  $N,$  or  $l, m,$  and  $n$  around the centroid of the spacecraft at  
 145 the central time of the time segment, we can use the constant velocity to calculate the  
 146 coordinates of the spacecraft at earlier or later times. Then we can get a best fit to all  
 147 the data, 24 equations for each observation time plus the four  $\nabla \cdot \mathbf{B} = \mathbf{0}$  conditions.  
 148 In practice, we start with a guess for the velocity using the STD method, and then use  
 149 a nonlinear minimization routine (Matlab `fminsearch`) to find the velocity that minimizes  
 150 the squared difference between the model and the observations.

151 Like Denton et al. (2020), we normalize distances to the average spacecraft spac-  
 152 ing  $d_{sc}.$  Then  $\mathbf{B}$  and  $\mu_0 \mathbf{J} = \nabla \times \mathbf{B}$  have the same units for the least-squares calcula-  
 153 tion. We also satisfy  $\nabla \cdot \mathbf{B} = \mathbf{0}$  exactly. Using the complete quadratic expansion in  
 154 equations (1), there is no need to rotate to the MDD coordinates, as was done by Torbert  
 155 et al. (2020) and Denton et al. (2020, 2021). However, we also consider solutions using  
 156 reduced sets of equations with fewer terms (Denton et al., 2020). In that case, we nor-  
 157 mally evaluate the solution for each data time segment (set of observation times) in the  
 158 MDD  $l$ - $m$ - $n$  frame of the central time value of that time segment. Then the resulting  
 159 reconstructed fields are rotated back to the  $L$ - $M$ - $N$  coordinate system for comparison  
 160 to the simulation or MMS data.

161 Denton et al. (2020) called a model that neglected  $\partial^2 B_i / \partial m^2$  terms, but kept all  
 162 the other terms in the quadratic expansion, “full quadratic”, and abbreviated the name  
 163 of the model as Q-3D. This model has the same equations as equations (1) neglecting  
 164 the  $\partial^2 B_i / \partial M^2$  terms, but with  $M, L,$  and  $N$  replaced by  $m, l,$  and  $n,$  respectively. To  
 165 avoid confusion with our past nomenclature, we will abbreviate the name of the “com-

**Table 1.** Characteristics of reconstruction models

Model	Abbreviation	Uses $\mathbf{J}$ as input	$\partial^2/\partial m^2$	$\partial^2/\partial m\partial n$ $\partial^2/\partial m\partial l$	$\partial/\partial m$	$\partial^2 B_n/\partial n^2$ $\partial^2 B_l/\partial l^2$ $\partial^2 B_n/\partial n\partial l$ $\partial^2 B_l/\partial n\partial l$
3D Complete Quadratic	CQ-3D	Yes	Yes	Yes	Yes	Yes
3D Quadratic	Q-3D	Yes	No	Yes	Yes	Yes
3D Reduced Quadratic	RQ-3D	Yes	No	No	Yes	No
3D Linear with only $\mathbf{B}$ as input	LB-3D	No	No	No	Yes	No
2D models	-2D	Depends <sup>a</sup>	No	No	No	Depends <sup>a</sup>

<sup>a</sup>Depends on the particular model.

166 plete quadratic” model in equations (1) as CQ-3D, and maintain the same model abbrevi-  
 167 viations for the “full quadratic”, “reduced quadratic”, and linear models as were used  
 168 by Denton et al. (2020), Q-3D, RQ-3D, and LB-3D respectively. In terms of the local  
 169 MDD coordinates,  $m$ ,  $l$ , and  $n$ , the equations of the 3D reduced quadratic (RQ-3D) are

$$B_l = B_{l,0} + \frac{\partial B_l}{\partial n}n + \frac{\partial B_l}{\partial l}l + \frac{\partial B_l}{\partial m}m + \frac{\partial^2 B_l}{\partial n^2} \frac{n^2}{2} \quad (2)$$

$$B_m = B_{m,0} + \frac{\partial B_m}{\partial n}n + \frac{\partial B_m}{\partial l}l + \frac{\partial B_m}{\partial m}m + \frac{\partial^2 B_m}{\partial n^2} \frac{n^2}{2} + \frac{\partial^2 B_m}{\partial n\partial l}nl + \frac{\partial^2 B_m}{\partial l^2} \frac{l^2}{2} \quad (3)$$

$$B_n = B_{n,0} + \frac{\partial B_n}{\partial n}n + \frac{\partial B_n}{\partial l}l + \frac{\partial B_n}{\partial m}m + \frac{\partial^2 B_n}{\partial l^2} \frac{l^2}{2}, \quad (4)$$

170 in addition to a single equation for  $\nabla \cdot \mathbf{B} = \mathbf{0}$ .

171 We also consider a linear model, “LB-3D” (Denton et al., 2020), with

$$B_i = B_{i,0} + \frac{\partial B_i}{\partial L}L + \frac{\partial B_i}{\partial M}M + \frac{\partial B_i}{\partial N}N, \quad (5)$$

172 in addition to a single equation for  $\nabla \cdot \mathbf{B} = \mathbf{0}$ . This is essentially the same model as  
 173 the FOTE model of Fu et al. (2015).

174 All of these models include at least a linear dependence on  $m$ , and so are three-  
 175 dimensional. 2D versions of these models, Q-2D, RQ-2D, and LB-2D, eliminate all  $m$ -  
 176 dependent terms from the 3D versions (Denton et al., 2020). (A 2D version for the CQ-  
 177 3D model would be the same as Q-2D, since these models only differ because of the  $\partial^2 B_i/\partial m^2$   
 178 terms.) Table 1 summarizes the characteristics of the various models discussed in this  
 179 paper. The terms in the header of Table 1 are expressed using  $l$ - $m$ - $n$  coordinates, but  
 180 all the models can also be evaluated in terms of  $L$ - $M$ - $N$  coordinates, and we will explore  
 181 that option below.

### 182 3 Reconstruction of simulation data

#### 183 3.1 Simulation data

184 The simulation data that we will use are from the particle in cell simulation of sym-  
 185 metric (across the current sheet) magnetic reconnection by Liu et al. (2019). The pur-  
 186 pose of this simulation was to study how magnetic reconnection develops when the re-  
 187 gion of a thin current sheet is limited in the reconnection  $M$  direction (the “out of plane”  
 188 direction normal to the reconnection  $L$ - $N$  plane). A two-dimensional reconnection plane

189 contains an X point, which is the magnetic null in the  $B_L$  and  $B_N$  components. In three  
 190 dimensions, the X point is extended into an X line in the  $M$  direction.

191 Figure 1 shows the magnetic field at three different values of  $M$ . Because the sim-  
 192 ulation data files are so big, time-resolved field data were not saved, so we are using a  
 193 snapshot of the simulation fields at one time. Four virtual spacecraft move through the  
 194 simulation with a velocity  $(3, 2, 1) d_i$  in  $L$ - $M$ - $N$  coordinates, where  $d_i$  is the ion iner-  
 195 tial length  $\equiv c/\omega_{\text{pi}} = \sqrt{\frac{m_i}{n_i e^2 \mu_0}}$ , where  $\omega_{\text{pi}}$  is the ion (or proton) plasma frequency,  $m_i$   
 196 is the ion mass,  $n_i$  is the ion density,  $e$  is the proton charge,  $\mu_0$  is the magnetic vacuum  
 197 permeability, and time is dimensionless. Since the velocity is constant, the time of flight  
 198 of our virtual spacecraft corresponds directly to distance traveled. We use the  $N$  coord-  
 199 inate for the time. That is, at  $t = 0$ ,  $N = 0 d_i$ , indicating that the centroid of the  
 200 spacecraft is at center of the current sheet.

201 The virtual spacecraft move along the diagonal lines from the bottom left to top  
 202 right in Figure 1; the colored circles show the positions of the spacecraft in each panel.  
 203 At the same time, they are moving into the page, that is, in the positive  $M$  direction.  
 204 Here only,  $L$ ,  $M$ , and  $N$  are measured relative to the fixed center of the simulation; else-  
 205 where, they will be measured from the centroid of the virtual spacecraft. The field in each  
 206 panel corresponds to the field at the  $M$  value of the centroid of the spacecraft, so that  
 207 the centroid  $M$  value is greater for Figure 1c ( $-5.5 d_i$ ) than for Figure 1a ( $-12.5 d_i$ ). Note  
 208 that at  $L = 0$ , the current sheet is thicker in Figure 1a, and the reconnection has pro-  
 209 gressed less, as indicated by the smaller island width on the left and right sides of the  
 210 plot and the smaller values of  $B_M$ . There is also difference in the structure of  $B_M$  as  $M$   
 211 is varied (comparing Figure 1a to Figure 1c). So the virtual spacecraft are moving through  
 212 a structure that is really three-dimensional, though the gradient in the  $M$  direction is  
 213 significantly smaller than that in the reconnection plane.

214 The simulation proton to electron mass ratio was 75. The simulation grid point spac-  
 215 ing was  $0.04 d_i$  and the separation between the virtual spacecraft is significantly larger,  
 216  $0.5 d_i$ .

217 At each point in time, the magnetic field and current density are determined for  
 218 each of the four virtual spacecraft. As we have done for our previous reconstructions of  
 219 MMS data (Torbert et al., 2020; Denton et al., 2020, 2021), we initially smoothed the  
 220 virtual spacecraft data using a boxcar average over a time interval (or displacement in  
 221  $N$ )  $t_{\text{smooth}}$ . The amount of smoothing can make a significant difference in the results.  
 222 In this study, we considered three choices,  $t_{\text{smooth}} = 0.4, 0.8$ , and  $1.6$ . Figure 2 shows  
 223 the effects of smoothing on the fields. Note that in figures such as Figure 2 with two-  
 224 part labels, e.g., “(Aa)”, the uppercase letter (here “A”) refers to a row of panels, whereas  
 225 the lowercase letter (here “a”) refers to a column of panels. Broadening of  $\mathbf{B}$  and broad-  
 226 ening and decrease of the magnitude of  $\mathbf{J}$  occurs with greater smoothing (progressing  
 227 from Figures 2A to 2D and from Figures 2E to 2H). These effects are minimal for  $t_{\text{smooth}} =$   
 228  $0.4$ , but substantial for  $t_{\text{smooth}} = 1.6$ .

229 Figure 3 shows the eigenvectors of MDD and Minimum Gradient Analysis (MGA)  
 230 (Shi et al., 2005, 2019). This plot is made for  $t_{\text{smooth}} = 0.8$ , but the results of MDD  
 231 and MGA do not depend greatly on the smoothing (not shown). Both MDD and MGA  
 232 use the matrix  $\nabla \mathbf{B}$  calculated from the instantaneous data from four spacecraft (here  
 233 virtual) to find eigenvectors, but MDD calculates the maximum, intermediate, and min-  
 234 imum gradient directions,  $\mathbf{e}_n$ ,  $\mathbf{e}_l$ , and  $\mathbf{e}_m$ , respectively, whereas MGA finds the maximum,  
 235 intermediate, and minimum variance (“MVA-like”) directions,  $\mathbf{e}_{l,MGA}$ ,  $\mathbf{e}_{m,MGA}$ , and  $\mathbf{e}_{n,MGA}$ ,  
 236 respectively. The  $L$ ,  $M$ , and  $N$  directions that we used were the original axes of the sim-  
 237 ulation ( $x$ ,  $y$ , and  $z$ , respectively, of Liu et al. (2019)). These directions differ at most  
 238 by  $2^\circ$  from those calculated using the method of Denton et al. (2018) that makes use of  
 239 the maximum gradient direction for  $\mathbf{e}_N$  and the maximum variance direction for  $\mathbf{e}_L$ .

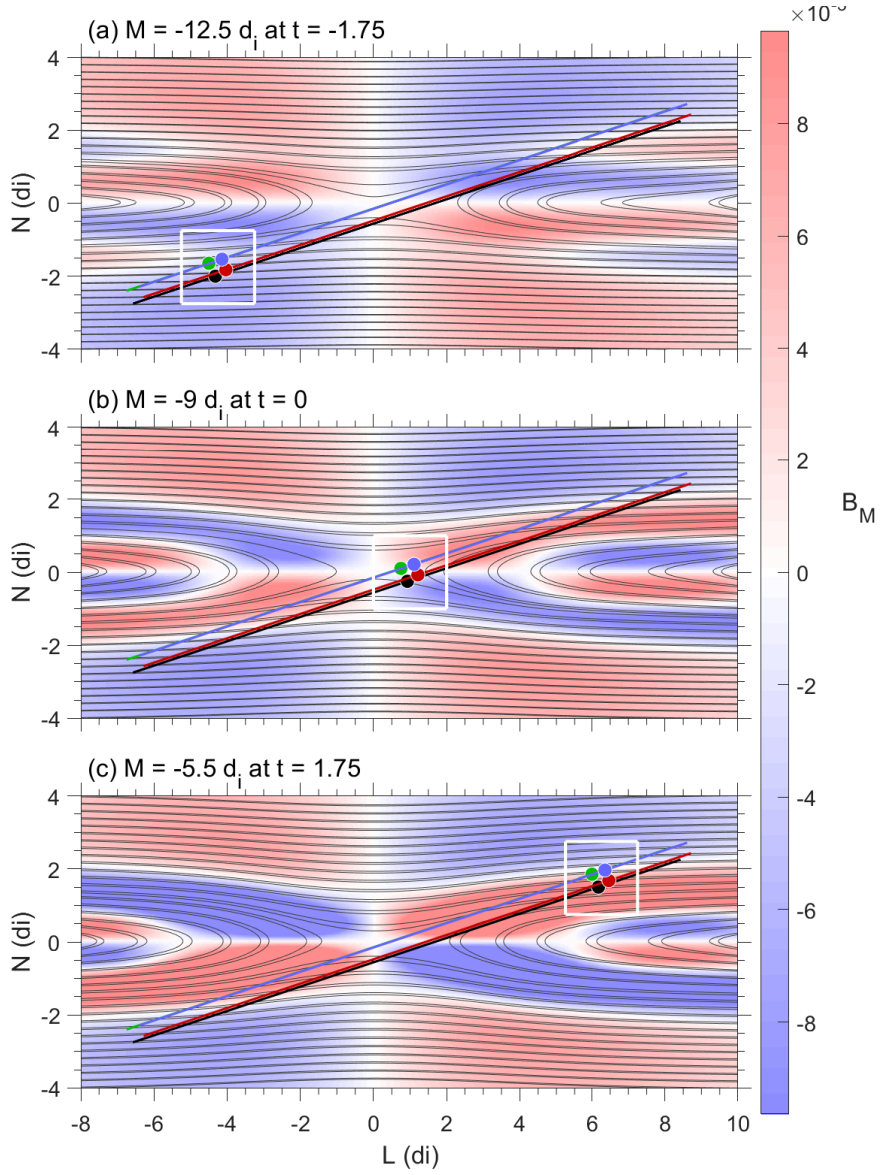


**Figure 1.** Magnetic field from the simulation of Liu et al. (2019). (a–c) show the simulation magnetic field at (a)  $M = -12.5 d_i$  at time  $t = -1.75$ , (b)  $M = -9 d_i$  at time  $t = 0$ , and (c)  $M = -5.5 d_i$  at time  $t = 1.75$ , where  $M$  was measured relative to the central  $M$  value of the simulation. Streamlines of the  $L$  and  $N$  components of the magnetic field in the  $L$ - $N$  plane are shown by the black curves. The color scale shows  $B_M$ , which is small compared to the reconnection magnetic field  $\sim 0.25$  (in the simulation normalization). The diagonal lines show the trajectories of virtual spacecraft, with black, red, green, and blue corresponding to spacecraft 1, 2, 3, and 4. The circles, using the same colors, show the positions of the spacecraft at the time  $t$  when the centroid of the spacecraft is at the  $M$  values listed above. Thus the spacecraft are moving in the positive  $L$ ,  $N$ , and  $M$  directions relative to the magnetic structure.

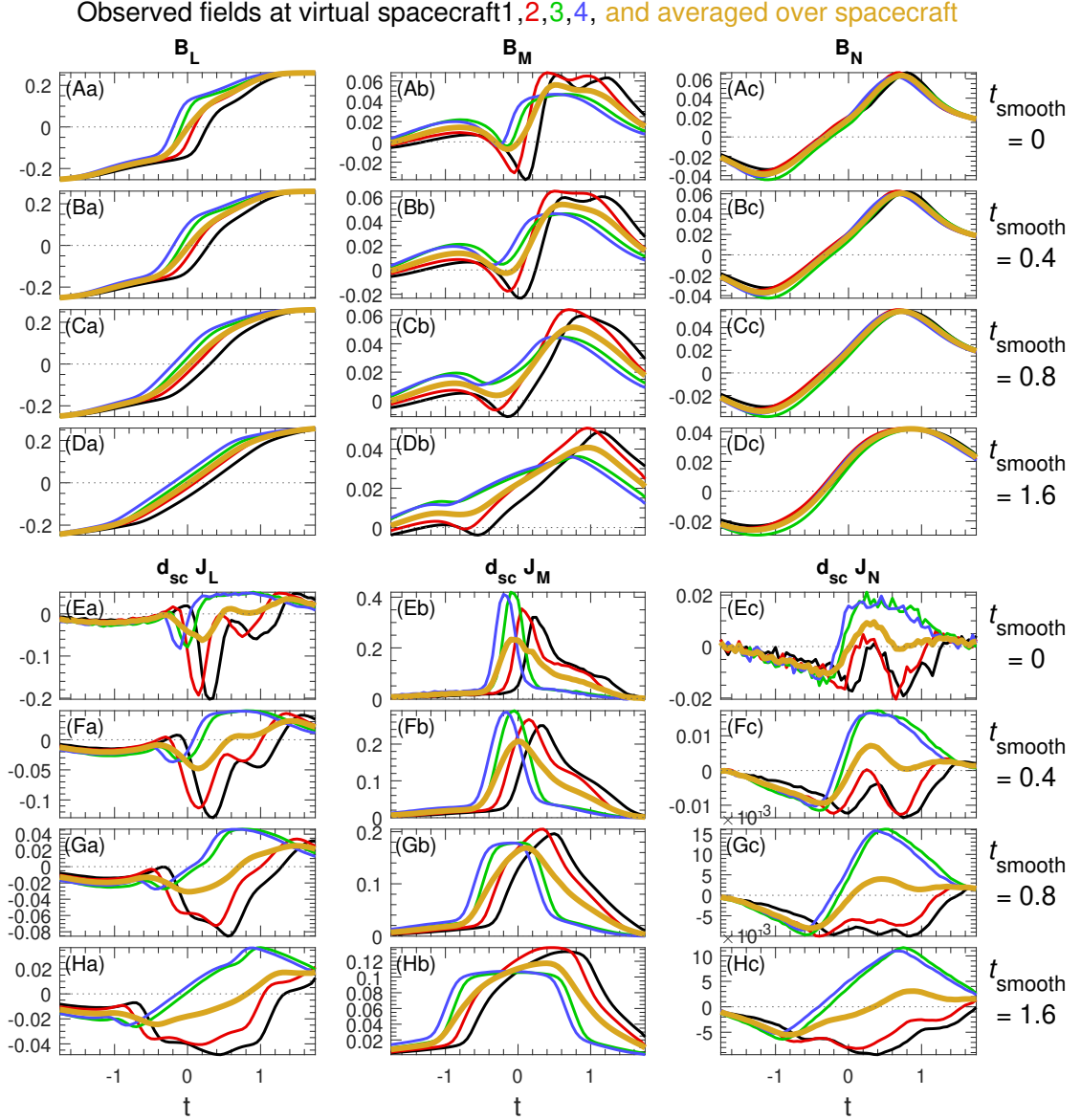


**Figure 2.** Input data to the reconstruction of simulation data showing the effects of smoothing. The (a)  $L$ , (b)  $M$ , and (c)  $N$  components of (A–D) the magnetic field  $\mathbf{B}$ , and (E–H) the product of the current density,  $\mathbf{J}$ , and the spacecraft spacing  $d_{\text{sc}}$ . In the simulation,  $d_{\text{sc}}\mathbf{J}$  has the same units as  $\mathbf{B}$ . The time intervals for boxcar smoothing of the input data are shown at the right of panels c;  $t_{\text{smooth}} = 0$  indicates no smoothing (raw data).

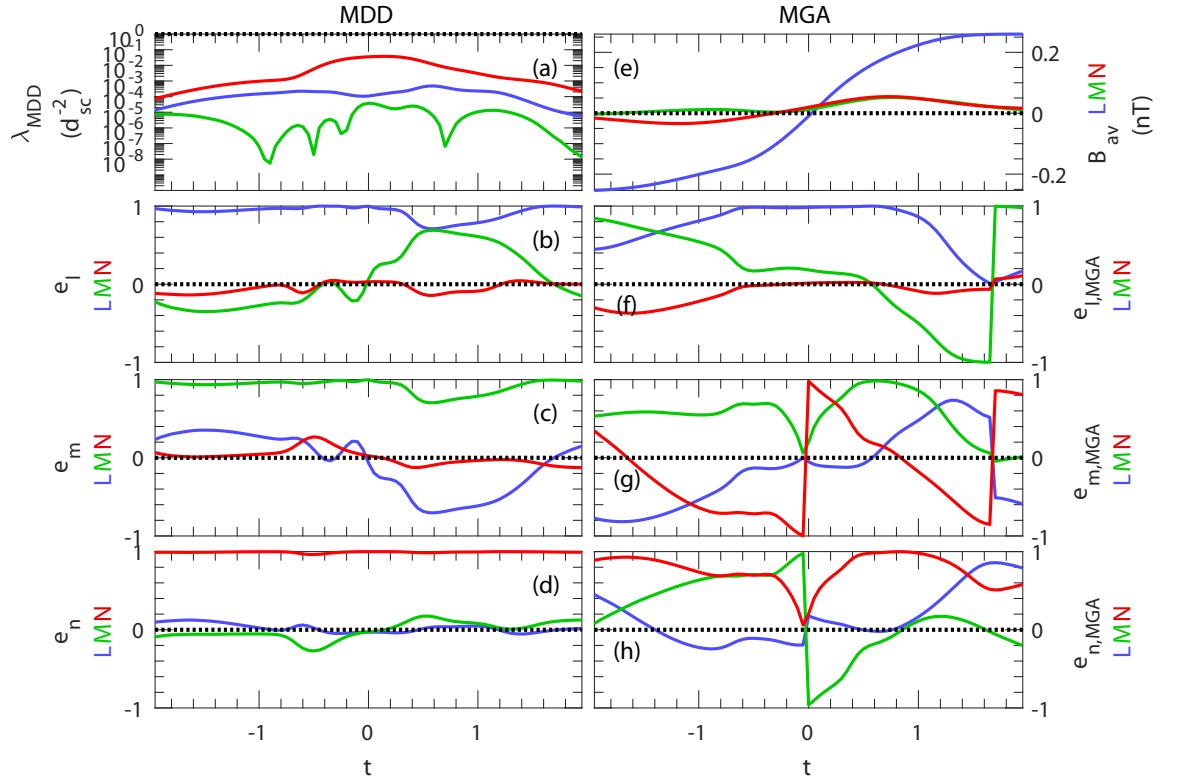


**Figure 3.** MDD and MGA results for simulation data. (a) MDD or MGA eigenvalues; (b–d)  $L$ ,  $M$ , and  $N$  components of the MDD local gradient directions (b)  $\mathbf{e}_l$ , (c)  $\mathbf{e}_m$ , and (d)  $\mathbf{e}_n$ ; (e) magnetic field components averaged over the four virtual spacecraft; and (f–h) MGA eigenvector directions.

Figure 3e shows the magnetic field averaged over the four spacecraft for context. The maximum gradient eigenvalue, equal to the square of the maximum gradient of the magnetic field (red curve in Figure 3a), is largest at the current sheet crossing where  $B_{\text{av},L}$  (blue curve in Figure 3e) reverses sign;  $B_{\text{av},N}$  reverses sign sooner but close to the time of the  $B_{\text{av},L}$  reversal (red curve in Figure 3e), showing that the spacecraft are passing close to the X line (Figure 1). Note the asymmetry in  $B_{\text{av},M}$  on the two sides of the current sheet, which is because the spacecraft passed to the right of the X line in Figure 1.

For much of the time, especially  $t < 0$  and  $t > 1.6$ ,  $\mathbf{e}_l$ ,  $\mathbf{e}_m$ , and  $\mathbf{e}_n$  are close to  $\mathbf{e}_L$ ,  $\mathbf{e}_M$ , and  $\mathbf{e}_N$  (Figures 3b–3d). For  $0.1 < t < 1.5$ , however,  $\mathbf{e}_m$  is significantly different from  $\mathbf{e}_M$ , with a significant contribution from  $\mathbf{e}_L$ , as has sometimes been observed for MMS data (Denton et al., 2016, 2018). This confirms that the simulation is truly three-dimensional, although the gradients are smaller in the  $M$  direction.

The correspondence of  $\mathbf{e}_{l,MGA}$ ,  $\mathbf{e}_{m,MGA}$ , and  $\mathbf{e}_{n,MGA}$  with  $\mathbf{e}_L$ ,  $\mathbf{e}_M$ , and  $\mathbf{e}_N$  is not as strong, though for a significant portion of the time,  $-0.6 < t < 0.7$ ,  $\mathbf{e}_{l,MGA}$  is fairly close to  $\mathbf{e}_L$ .

### 3.2 Simulation reconstruction cases

We reconstructed the simulation magnetic field using the variations of method summarized in Table 2. The set of equations used in the model is indicated in the second column of Table 2. “Yes” in the fifth column of Table 2 with the “ $l$ - $m$ - $n$ ?” header indicates that the local (time-dependent) MDD  $l$ - $m$ - $n$  coordinate system was used for the reconstruction. The RQ-3D and Q-3D models are normally calculated in the local  $l$ - $m$ - $n$  coordinate system, whereas the CQ-3D model is calculated in the fixed  $L$ - $M$ - $N$  coordinate system. With the complete quadratic expansion, the results are independent of the coordinate system. The same is true of the linear model, LB-3D, so we could have calculated that in the  $L$ - $M$ - $N$  coordinate system also. But we can calculate any of these models in either coordinate system. Results are always shown in the  $L$ - $M$ - $N$  coordinate system.

Cases 1–3 examine differences in results because of different smoothing. Cases 1, 2, and 3 use the RQ-3D model with  $t_{\text{smooth}} = 0.4, 0.8,$  and  $1.6$ , respectively (third column of Table 2). In cases 1–3, we use observations at multiple times over an interval  $t_{\text{input}} = t_{\text{smooth}}/2$  (fourth column of Table 2). The resolution of the data is  $0.05$ , so the number of data points used as input to the model is  $t_{\text{input}}/0.05 + 1$ . For  $t_{\text{input}} = 0.2$ , five data points are used. Using  $t_{\text{input}} = t_{\text{smooth}}/2$  does not effectively increase the amount of smoothing, and yields slightly better reconstructions than are found using fewer observation times (not shown).

Cases 4–6 show results using input data from a single time (Denton et al., 2020), so  $t_{\text{input}} = 0$ .

Using the multiple-time input method with a finite time interval, we solve for the structure velocity. The velocity is listed in the rightmost 3 columns of Table 2; the notation “NA” for not applicable indicates that the velocity component is not calculated. For cases 1–3 and 7–10, we solve only for the  $l$  and  $n$  (for RQ-3D or Q-3D models) or  $L$  and  $N$  (for the CQ-3D model) components of the velocity. This choice is indicated in the fifth column of Table 2 labeled “ $v_{m/M}$ ?”, where “No” in that column indicates that the  $m$  or  $M$  component is not calculated. The motivation for not calculating the  $m$  or  $M$  component is that that component of the calculated velocity is not very accurate, as we will show below. Although we calculate  $l$  and  $n$  components of the structure velocity for the RQ-3D and Q-3D methods, we convert these to  $L$ ,  $M$ , and  $N$  components for the purposes of comparing to the known structure velocity. Thus for the RQ-3D or Q-3D models, we find a small velocity component in the  $M$  direction (e.g., Table 2, case 8),

**Table 2.** Simulation reconstruction cases

Case	Model	$t_{\text{smooth}}^a$	$t_{\text{input}}^b$	$l-m-n^c$	$v_{\text{str},m}/M^?d$	$dB_{\text{err},\text{av}}^e$ ( $R = 0.35d_{\text{sc}}$ )	$dB_{\text{err},\text{av}}^e$ ( $R = 1d_{\text{sc}}$ )	$dB_{\text{err},\text{av}}^e$ ( $R = 2d_{\text{sc}}$ )	Median velocity from polynomial reconstruction <sup>f</sup>	$v_{\text{str},M}$	$v_{\text{str},N}$
1	RQ-3D	0.4	0.2	Yes	No	0.099	0.14	0.61	-2±0.88	-0.012±0.7	-0.9±0.2
2	RQ-3D	0.8	0.4	Yes	No	0.18	0.15	0.33	-2.2±0.67	-0.029±0.8	-0.93±0.18
3	RQ-3D	1.6	0.8	Yes	No	0.29	0.25	0.25	-2.2±0.81	-0.15±0.93	-0.85±0.18
4	LB-3D	0.8	0	Yes	NA	0.19	0.19	0.36	NA	NA	NA
5	RQ-3D	0.8	0	Yes	NA	0.18	0.15	0.38	NA	NA	NA
6	Q-3D	0.8	0	Yes	NA	0.18	0.18	0.55	NA	NA	NA
7	LB-3D	0.8	0.4	Yes	No	0.2	0.19	0.34	-2.2±0.6	0.0019±0.81	-0.96±0.13
8 (=2)	RQ-3D	0.8	0.4	Yes	No	0.18	0.15	0.33	-2.2±0.67	-0.029±0.8	-0.93±0.18
9	Q-3D	0.8	0.4	Yes	No	0.18	0.15	0.36	-2.3±0.44	-0.033±1.1	-0.96±0.12
10	CQ-3D	0.8	0.4	No	No	0.18	0.16	0.4	-2.3±0.47	NA	-0.98±0.1
11	LB-3D	0.8	0.4	Yes	Yes	0.2	0.19	0.34	$-1.5 \times 10^{11} \pm 3.8 \times 10^{12}$	$5.4 \times 10^{11} \pm 1.3 \times 10^{13}$	$-1.3 \pm 8.9 \times 10^{11}$
12	RQ-3D	0.8	0.4	Yes	Yes	0.18	0.15	0.35	$-2.5 \pm 1.3 \times 10^{12}$	$-4.9 \pm 4.3 \times 10^{12}$	$-0.89 \pm 1.9 \times 10^{11}$
13	Q-3D	0.8	0.4	Yes	Yes	0.18	0.15	0.37	-2.6±0.35	0.98±1.5	-1.1±0.093
14	CQ-3D	0.8	0.4	No	Yes	0.18	0.15	0.38	-2.5±0.38	0.83±1.5	-1.1±0.098
15	LB-3D	0.8	0.4	No	No	0.2	0.19	0.34	-2.5±0.39	NA	-1±0.086
16	RQ-3D	0.8	0.4	No	No	0.18	0.15	0.32	-2.3±0.4	NA	-0.94±0.12
17	Q-3D	0.8	0.4	No	No	0.18	0.15	0.36	-2.5±0.45	NA	-1±0.1
18 (=10)	CQ-3D	0.8	0.4	No	No	0.18	0.16	0.4	-2.3±0.47	NA	-0.98±0.1
19	LB-2D	0.8	0.4	Yes	No	0.2	0.19	0.34	-2.2±0.49	-0.0055±0.85	-0.96±0.13
20	RQ-2D	0.8	0.4	Yes	No	0.18	0.15	0.34	-1.8±0.64	-0.04±0.71	-0.97±0.18
21	Q-2D	0.8	0.4	Yes	No	0.18	0.16	0.35	-2.2±0.5	-0.041±1.1	-1±0.073
22	LB-2D	0.8	0.4	No	No	0.2	0.19	0.33	-2.4±0.42	NA	-1±0.096
23	RQ-2D	0.8	0.4	No	No	0.18	0.15	0.32	-2.3±0.47	NA	-0.92±0.084
24	Q-2D	0.8	0.4	No	No	0.18	0.15	0.32	-2.6±0.32	NA	-0.98±0.055
25 (=7)	LB-3D	0.8(+Sim) <sup>e</sup>	0.4	Yes	No	<b>0.2</b>	<b>0.19</b>	<b>0.34</b>	-2.2±0.6	0.0019±0.81	-0.96±0.13
26 (=8)	RQ-3D	0.8(+Sim) <sup>e</sup>	0.4	Yes	No	<b>0.062</b>	<b>0.075</b>	<b>0.31</b>	-2.2±0.67	-0.029±0.8	-0.93±0.18
27 (=9)	Q-3D	0.8(+Sim) <sup>e</sup>	0.4	Yes	No	<b>0.059</b>	<b>0.085</b>	<b>0.35</b>	-2.3±0.44	-0.033±1.1	-0.96±0.12
28 (=10)	CQ-3D	0.8(+Sim) <sup>e</sup>	0.4	No	No	<b>0.18</b>	<b>0.16</b>	<b>0.4</b>	-2.3±0.47	NA	-0.98±0.1

<sup>a</sup>Time interval (or  $N$  displacement) for smoothing of spacecraft **B** and **J** as input to model

<sup>b</sup>Time interval (or  $N$  displacement) for input to the model; 0 for method of Denton et al. (2020); the number of data points used as input to the model is  $t_{\text{input}}/0.05 + 1$

<sup>c</sup>“Yes” indicates that we rotate into the  $l-m-n$  coordinate system to calculate the reconstruction parameters

<sup>d</sup>“Yes” indicates that the  $m$  or  $M$  velocity component is calculated; “NA” (not applicable) if no velocity components are calculated

<sup>e</sup>Error parameter defined in (6) averaged from  $t = -0.4$  to  $0.4$  at radius indicated; for cases 25-28, it is calculated with smoothed simulation data as described in the text

<sup>f</sup>The exact velocity is  $(v_{\text{str},L}, v_{\text{str},M}, v_{\text{str},N}) = (-3, -2, -1)$ ; “NA” (not applicable) for velocity components not calculated

289 but not for the CQ-3D model that is calculated using an expansion in the  $L$ ,  $M$ , and  $N$   
 290 coordinates (e.g., Table 2, case 10).

291 For cases 11-14, we solve for the three-dimensional structure velocity, as indicated  
 292 by “Yes” in the sixth column of Table 2 labeled “ $v_{str,m/M}$ ?”.

293 Cases 15–18 are like cases 7–10 (multiple times for input, but not calculating the  
 294  $m$  or  $M$  velocity component), except that all the models (even RQ-3D and Q-3D) are  
 295 evaluated in the  $L$ - $M$ - $N$  coordinate system, as indicated by “No” in the fifth column of  
 296 Table 2 with the “ $l$ - $m$ - $n$ ?” header. So for the Q-3D model, for instance, the  $\partial^2 B_i / \partial M^2$   
 297 rather than  $\partial^2 B_i / \partial m^2$  dependence is not included in the model.

298 Cases 19–21 show results for 2D versions of the models. Cases 19–21 are evaluated  
 299 in the  $l$ - $m$ - $n$  coordinate system as indicated by “No” in the fifth column of Table 2 with  
 300 the “ $l$ - $m$ - $n$ ?” header. So for these cases, none of the models have any  $m$  dependence. Cases 22–  
 301 24 are similar except evaluated in the  $L$ - $M$ - $N$  coordinate system, so that none of the mod-  
 302 els have any  $M$  dependence.

303 The seventh, eighth, and ninth columns of Table 2 show the average (mean) error  
 304 parameter  $dB_{err,av}$ , with

$$dB_{err} = \frac{|\mathbf{B}_{mod} - \mathbf{B}_{sim}|}{B_{sim,max}}, \quad (6)$$

305 at three radial distances from the centroid of the spacecraft positions, where  $\mathbf{B}_{mod}$  is the  
 306 reconstruction model field,  $\mathbf{B}_{sim}$  is the simulation field, and  $B_{sim,max}$  is the maximum  
 307 magnitude of the simulation field in the reconstructed region, which has the shape of a  
 308 cube with  $L/d_{sc}$ ,  $M/d_{sc}$ , and  $N/d_{sc}$  varying from -2 to +2. Values of  $dB_{err,av}$  are shown  
 309 for radii of  $0.35d_{sc}$ ,  $1d_{sc}$ , and  $2d_{sc}$  from the centroid of the spacecraft within the three-  
 310 dimensional volume. The averaging is done over different locations at the radii specified  
 311 (roughly within a spherical shell of width  $0.1 d_{sc}$ ) and over the time interval  $t = -0.4$   
 312 to  $0.4$ . That is the time interval over which the errors are greatest. For a perfect recon-  
 313 struction, the values of  $dB_{err,av}$  would be zero. A value of  $dB_{err,av}$  equal to unity would  
 314 mean that the reconstructed magnetic field is far from the simulation field. The radius  
 315  $0.35d_{sc}$  is less than the distance to the individual spacecraft at  $0.61d_{sc}$  and within the  
 316 spacecraft tetrahedron. The radius of  $1d_{sc}$  is outside the spacecraft tetrahedron, and the  
 317 distance  $2d_{sc}$  is significantly farther away.

318 Cases 25–28 in Table 2 are the same as cases 7–10 except that  $dB_{err,av}$  is calculated  
 319 using spatially smoothed simulation data, as described in section 5.7. So the only dif-  
 320 ferent numbers in Table 2 for cases 25–28 are the boldface numbers showing  $dB_{err,av}$  val-  
 321 ues.

### 322 3.3 Reconstruction results considering differences in smoothing

323 Figure 4 compares model (solid curves) and the smoothed virtual spacecraft data  
 324 (dotted curves) components of  $\mathbf{B}$  and  $d_{sc}\mathbf{J}$  for simulation reconstruction case 2 in Ta-  
 325 ble 2. This case used the RQ-3D model with  $t_{smooth} = 0.8$  and  $t_{input} = 0.4$  and solved  
 326 for the three-dimensional structure velocity without calculation of  $v_{str,m}$ . Comparing the  
 327 solid and dotted curves, the data was fairly well described by the model. The agreement  
 328 is least good for  $J_N$ , but note that the values of  $J_N$  are very small. Other cases using  
 329 the RQ-3D model show comparable agreement. Much better agreement is achieved with  
 330 the Q-3D and CQ-3D models because of the greater number of parameters in those mod-  
 331 els.

332 Agreement of the model and simulation fields at the spacecraft positions, as shown  
 333 in Figure 4, is a consistency check for the model, but it does not show that the recon-  
 334 structions accurately represent the simulation fields away from the spacecraft positions.

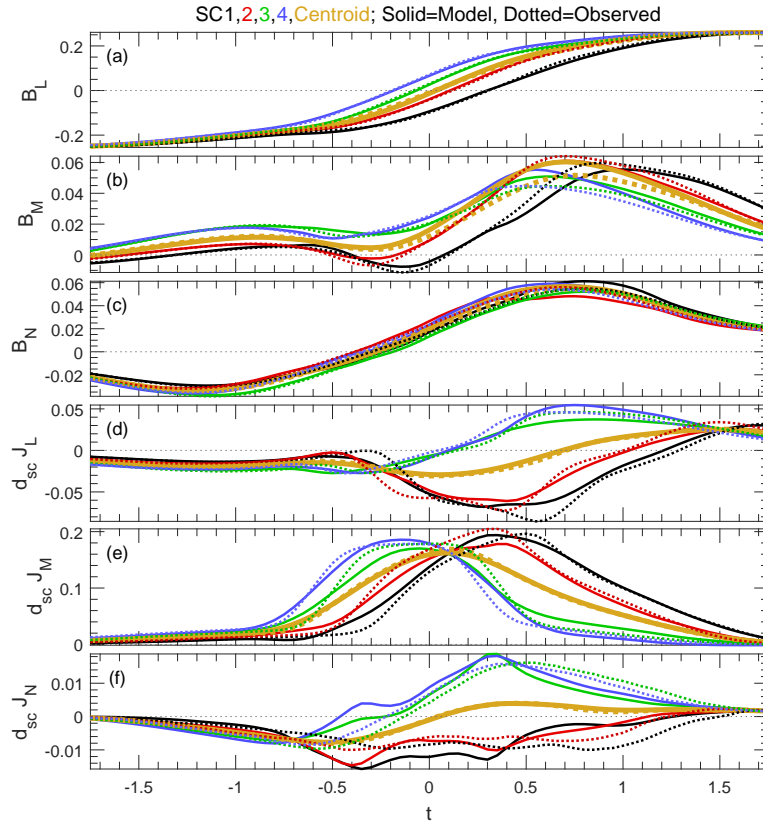


**Figure 4.** Comparison of model and virtual spacecraft data. Model (solid) and virtual spacecraft data (dotted) (a–c) magnetic field and (d–f) current density components multiplied by  $d_{sc}$  for simulation reconstruction case 2 in Table 2.

Figure 5. Reconstruction magnetic field in the L-N plane for reconstruction case 1. (a) Magnetic field averaged over the four virtual spacecraft,  $B_{av}$ , versus time showing the times of the two-dimensional representations of the magnetic field in panels b-q. (b-q) Reconstructed magnetic streamlines in the L-N plane (black) and magnetic field into the plane of the page,  $B_M$  (color scale). The positions of the virtual spacecraft relative to the spacecraft centroid (origin of each panel) are indicated by the black, red, green, and blue circles for spacecraft 1, 2, 3, and 4.

craft observations at the spacecraft locations (Denton et al., 2020). Using  $t_{\text{smooth}} = 0.4$  and  $t_{\text{input}} = 0.2$ , the Q-3D model does yield a small value of  $dB_{\text{err,av}} = 0.092$  inside the tetrahedron at  $R = 0.35d_{\text{sc}}$  (case not listed in Table 2). But the RQ-3D model yields almost the same value, 0.099 (case 1 in Table 2). And the Q-3D model with  $t_{\text{smooth}} = 0.4$  and  $t_{\text{input}} = 0.2$  yields values of  $dB_{\text{err,av}}$  that are significantly larger than those of the RQ-3D model at both  $R = 1d_{\text{sc}}$  and  $2d_{\text{sc}}$ , 0.21, and 0.95, respectively, compared to 0.14 and 0.61 for case 1.

### 3.5 Results for different models using multiple observation times for input

Cases 7–10 show results for the multiple-time input method but using different models. Note that case 8 is the same as case 2, but repeated in Table 2 for easier comparison to cases 7, 9, and 10. The errors are slightly smallest for case 8 (= case 2) for the RQ-3D model, though there is not a great difference in results as the model is varied. Figure 7 is like Figure 6, except for case 10 for the complete quadratic CQ-3D model. See also movie S5 for case 10 in the supplementary information. Figure 7 shows that it is possible to use a complete expansion by making use of the greater number of observations from a finite time interval.

In some respects, the reconstructions in the  $L$ - $N$  plane shown in Figure 7 for the CQ-3D model are more realistic than those in Figure 6 for the RQ-3D model. For instance, note that the reconstructed fields like the simulation fields in Figure 7c (top and bottom panels, respectively) do not include an O point and that the X line is to the left of the field-of-view for both reconstructed and simulation fields in Figure 7h. The CQ-3D model also has the advantage that no rotations are required.

The errors for case 10 as indicated by  $dB_{\text{err,av}}$  are somewhat greater than those for the RQ-3D model (case 8), but not much greater. As noted above, this is in contrast to the results using a single time of observation as input to the model, for which the errors at  $R = 2d_{\text{sc}}$  for the Q-3D model, omitting only the  $\partial^2 B_i / \partial m^2$  terms, were significantly greater than those of the RQ-3D model (comparing cases 5 and 6 in Table 2). Simply put, a model with more parameters requires more input data.

To get a better understanding of the errors from the model, we show in Figure 8 2D cuts through 3D space of  $B_L$ ,  $B_M$ , and  $B_N$  at  $t = -0.3$ , corresponding to Figure 6d. The reconstruction model fields are shown in Figures 8a, 8d, and 8g, the simulation fields are shown in Figures 8b, 8e, and 8h, and the model fields minus the simulation fields are shown in Figures 8c, 8f, and 8i. Figures 8j show the error parameter  $dB_{\text{err}}$ . The color scale in each panel can be interpreted using the color bars at the bottom of the plot. Note that the values of  $B_L$  are much larger than those of  $B_M$  and  $B_N$ , as indicated by the scales on the color bars.

Consider first the  $L$ - $N$  cuts in Figure 8B. Figures 8Ba–8Bc show that the model preserves the simulation gradient of  $B_L$  with respect to  $N$ , but the model gradient is broader. The simulation gradient of  $B_N$  with respect to  $L$  is not so large (Figure 8Bh), and at  $N = 0$ , the model  $B_N$  (Figure 8Bh) agrees with the simulation  $B_N$  (Figure 8Bg). But  $B_N$  varies too much with respect to  $N$  (Figure 8Bg). This may be related to the slight variation of the larger  $B_L$  with respect to  $L$ , so that  $B_N$  varies with  $N$  so as to make  $\nabla \cdot \mathbf{B}$  equal to zero. The fact that  $B_L = B_N = 0$  (white color in Figure 8) occurs at the same values of  $N$  and  $L$ , respectively, for both model and simulation (Figures 8Ba, 8Bb, 8Bg, and 8Bh), indicates that the model correctly predicts the position of the X line, as was already shown in Figure 6d.

Figures 8Bd and 8Be show a big difference between the model and simulation  $B_M$  in the  $L$ - $N$  plane. The model does not correctly represent the quadrupolar structure. This is understandable considering that the virtual spacecraft passed under the X line

**Figure 7.** Comparison of reconstruction and simulation magnetic field in the  $L$ - $N$  plane for simulation reconstruction case 10. This plot is like Figure 6, except for case 10.

and did not sample the upper left quadrant of Figure 8Be. Because of this, the model has a large  $N$  dependence in the  $M$ - $N$  plane (Figure 8Cd), whereas the simulation in that plane has  $B_M$  approximately equal to zero (Figure 8Ce).

The model also has significantly greater  $M$  dependence than the simulation. And the error parameter  $\delta B_{\text{err}}$  (Figures 8j) is nonzero even close to the centroid of the spacecraft positions (origin of panels in Figure 8j). These results suggest that reconstruction results should be interpreted cautiously, understanding that there may be significant errors, particularly involving dependence that is not well sampled by the spacecraft.

Figures S2{S5 in the Supplementary Information compare reconstruction and simulation fields for cases 7{10, respectively, using the format of Figure 6. Similarly, movies S2{S5 show the time variation of the reconstruction magnetic field for cases 7{10. Despite the differences in the error parameter  $\delta B_{\text{err};\text{av}}$  shown in Table 2, all of the models yield reasonable reconstruction results in the  $L$ - $N$  plane.

### 3.6 Velocity from the reconstruction

As previously mentioned, the exact structure velocity (relative to the spacecraft) used to create the virtual spacecraft data was  $(v_{\text{str};L}, v_{\text{str};M}, v_{\text{str};N}) = (-3, -2, -1)$ . For each case in Table 2 using the multiple-time input method (all cases other than 4{6), the method yields an estimate of the structure velocity (last 3 columns of Table 2).

Figure 9 shows the inferred velocity from the reconstruction (solid curves) versus time for case 2. We also show the velocity from the Spatio-Temporal Difference (STD) method Shi et al. (2006) (dotted curves). Clearly the velocities from the reconstruction and from STD are very similar.

For STD, we only calculated components of the velocity in the local  $l$  and  $m$  directions. For cases 1{3 and 7{10, we also assumed that the structure velocity only had  $l$  and  $n$  (or  $L$  and  $N$  for the CQ-3D model) components. Therefore the value of  $v_{\text{str};m}$  in Figure 9b is zero (dotted and solid curves). But the velocity components in the  $M$  direction are nonzero because  $e_l$  sometimes has a significant  $M$  component, as shown in Figure 3c. Nevertheless, the  $v_{\text{str};M}$  component cannot be accurate since it does not include a contribution from  $v_{\text{str};m}$ , and  $e_M$  is closer to  $e_m$  than to  $e_l$  or  $e_n$ .

Because of the large time variation of the calculated velocity, we chose to list median velocity values over the entire time interval  $-1.75$  to  $1.75$  in Table 2. For the reason mentioned in the last paragraph, the values of  $v_{\text{str};M}$  in the second to the last column of Table 2 are either inaccurate or not applicable for cases 1{3 and 7{10. The exact value of  $v_{\text{str};L}$  is  $-3$ , but all the estimates for cases 1{3 and 7{10 yield values between  $-2$  and  $-2.3$ . Looking at Figure 9d, the most inaccurate values of  $v_{\text{str};L}$  occur around  $t = 0.6$ , where  $e_L$  has a significant  $m$  component (Figure 3b), whereas more accurate values of  $v_{\text{str};L}$  (especially those from STD) occur at  $t = 0.4, 0$ , and  $1.7$ , where the  $m$  component of  $e_L$  is nearly zero.

Another possible cause of inaccuracy might be related to large nonlinearity of the fields. The most inaccurate values of  $v_{\text{str};L}$  in Figure 9d occur at  $t = 0.5$ , where the variation in  $J$  measured by the MMS spacecraft is greatest (Figure 4d{4f).

The estimates for  $v_{\text{str};N}$  are more accurate. The exact value should be  $-1$ , and the estimates range between  $-0.85$  and  $-0.98$ . It is not surprising that the most accurate component calculated is  $v_{\text{str};N}$ , because the gradient in the  $N$  direction is the best measured (Denton et al., 2021).

Cases 11{14 in Table 2 are like cases 7{10, except that the reconstruction method allows the structure velocity to have components in all three directions (as indicated by "Yes" in the sixth column of Table 2 labeled " $v_{\text{str};m=M}$ "). The resulting velocities are

531 event was that the MMS spacecraft passed mostly in the  $L$  direction right through the  
 532 X line (see their Figure 1k) with closest approach by MMS1. This is exactly what we  
 533 see in Figure 10. Note that in Figure 10k, MMS1 is very close to the X line. See movie S6  
 534 in the Supplementary Information for more detailed time dependence.

535 The inferred velocity for this event is shown in Figure 11. There are oscillations  
 536 in the  $L$  and  $N$  components, but these are most often negative with average values of  
 537  $v_L = -107$  km/s and  $v_N = -6.5$  km/s. At some times, especially between  $t = 24.6$   
 538 and  $25.4$  and between  $t = 25.8$  and  $26.3$ ,  $\mathbf{e}_m$  was almost exactly equal to  $\mathbf{e}_M$  (not shown).  
 539 At other times  $\mathbf{e}_m$  had contributions from both  $\mathbf{e}_M$  and  $\mathbf{e}_L$ . Therefore  $v_M$  cannot be de-  
 540 termined, and  $v_L$  will not be exactly accurate (see subsection 3.6). The multi-time in-  
 541 put method using the complete velocity (including  $v_m$ ) could not be used in this case  
 542 because the solution of the equations was numerically ill determined.

543 We saw in section 3.3 that the amount of smoothing could make a big difference  
 544 in reconstruction results. Figure 12 shows that the raw magnetic field data for the MMS  
 545 event exhibited larger fluctuations than the virtual spacecraft data for the simulation  
 546 (Figure 2). Smoothing of the MMS data with  $t_{\text{smooth}} = 0.5$  s smoothed out those mag-  
 547 netic fluctuations, but the smoothing of the current density (Figure 12D as compared  
 548 to Figure 12C) seems to be less than the smoothing that we recommended for the sim-  
 549 ulation data (Figure 2G as compared to Figure 2E).

550 The 27 August 2018 event was observed after the failure of two of the four FPI in-  
 551 strument sensors on MMS4, which occurred on 7 June 2018 at 12:43 UT. Because of that  
 552 failure, the current density cannot be reliably calculated for MMS4, reducing the amount  
 553 of input data. But because we used multiple observation times for input, and also be-  
 554 cause we used the RQ-3D model that has a reduced number of parameters, we were able  
 555 to do the reconstruction without the current density from MMS4 (as would not be pos-  
 556 sible for the Q-3D or Torbert et al. (2020) models using the fields for a single observa-  
 557 tion time as input).

## 558 4.2 Reconstruction of 7 December, 2016, MMS event

559 Now we use the multiple-time input method to reconstruct the magnetic field for  
 560 the 7 December 2016 magnetopause crossing described by Fuselier et al. (2019). This  
 561 event occurred at 05:19 UT at  $(X, Y, Z) = (9.6, 0.7, -0.5)$  Earth radii ( $R_E$ ) in Geocentric  
 562 Solar Ecliptic (GSE) coordinates, and the spacecraft were in a tetrahedron formation with  
 563 6.8 km average separation between the spacecraft, equal to  $0.14 d_i$  using the magnetosheath  
 564 density (Haaland et al., 2019). We used the coordinate system  $(L; M; N) = (0.29 -0.37$   
 565  $0.88 ; -0.08 -0.93 -0.36 ; 0.95 0.03 -0.30)$ , determined using the method of Denton et al.  
 566 (2018).

567 We again use  $t_{\text{smooth}} = 0.5$  s, and  $t_{\text{input}} = 0.24$  s (9 data points at 0.03 s resolu-  
 568 tion), allowing the magnetic structure to have only  $l$  and  $n$  velocity components. The  
 569 reconstructions in the  $L$ - $N$  plane are shown in Figure 13. Note that here the color scale  
 570 shows  $B_L$  rather than  $B_M$ , because that helps identify the current sheet crossing and  
 571 because  $B_M$  was fairly constant (Figure 13a, green curve). Fuselier et al.'s interpreta-  
 572 tion was that the MMS spacecraft were far (many  $R_E$ ) from the X line, and the purpose  
 573 of this example is to show that we do not always see X or O points in our reconstruc-  
 574 tions. Instead, the plot shows that the magnetic structure moves downward in Figures 13b-  
 575 13g, so that relative to that structure, the MMS spacecraft pass from the magnetosphere  
 576 (red color in Figures 13b-13e indicating positive  $B_L$ , where  $\mathbf{e}_L$  is approximately in the  
 577 GSE Z direction) through the current sheet (Figures 13i-13k) and into the magnetosheath  
 578 (blue color in Figures 13n-13q indicating negative  $B_L$ ). See movie S7 in the Supplemen-  
 579 tary Information for more detailed time dependence.

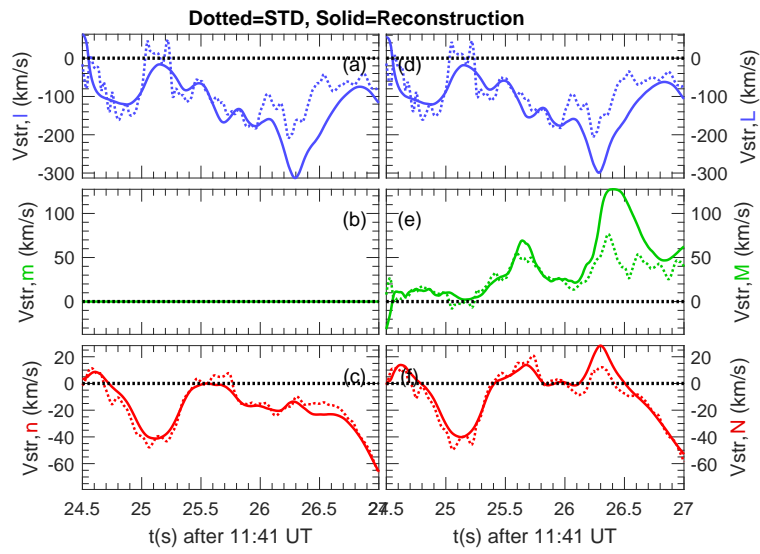


**Figure 11.** Inferred structure velocity for the MMS reconnection event observed on 27 August, 2018, using the same format as Figure 9.

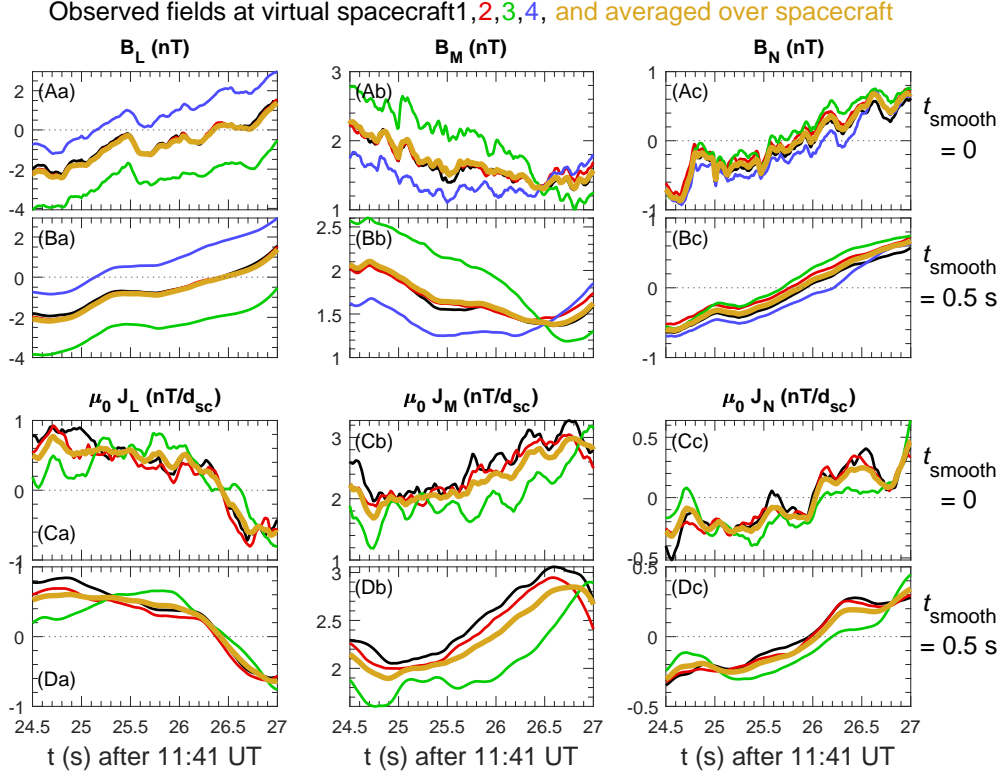


**Figure 12.** Input data to the reconstruction of data for MMS event on 27 August, 2018, showing the effects of the  $t_{\text{smooth}} = 0.5$  s smoothing used for the reconstruction. The (a)  $L$ , (b)  $M$ , and (c)  $N$  components of (A–B) the magnetic field  $\mathbf{B}$ , and (C–D)  $\mu_0 \mathbf{J}$  in units of  $nT/d_{\text{sc}}$ . (A and C) show the fields for the raw data without any smoothing, (B and D) show the fields with a boxcar smoothing time of  $t_{\text{smooth}} = 0.5$  s.

Figure 13. Reconstruction of the magnetic field for the magnetopause crossing event observed by MMS and described by Fuselier et al. (2019). This plot has the same format as Figure 5, except that the color shows  $B_L$  rather than  $B_M$ . The time is measured in s after 15:19 UT on 7 December, 2016.

- 928 A. (2006). Motion of observed structures calculated from multi-point magnetic  
929 field measurements: Application to Cluster. *Geophys. Res. Lett.*, *33*(8). doi:  
930 10.1029/2005gl025073
- 931 Shi, Q. Q., Tian, A. M., Bai, S. C., Hasegawa, H., Degeling, A. W., Pu, Z. Y., ...  
932 Liu, Z. Q. (2019). Dimensionality, Coordinate System and Reference Frame  
933 for Analysis of In-Situ Space Plasma and Field Data. *Space Science Reviews*,  
934 *215*(4). doi: 10.1007/s11214-019-0601-2
- 935 Sonnerup, B. U. O., Hasegawa, H., Teh, W. L., & Hau, L. N. (2006). Grad-  
936 Shafranov reconstruction: An overview. *J. Geophys. Res.*, *111*(A9). doi:  
937 10.1029/2006JA011717
- 938 Sonnerup, B. U. O., & Teh, W.-L. (2008). Reconstruction of two-dimensional co-  
939 herent MHD structures in a space plasma: The theory. *J. Geophys. Res.*,  
940 *113*(A5). doi: 10.1029/2007ja012718
- 941 Sonnerup, B. U. O., & Teh, W. L. (2009). Reconstruction of two-dimensional coher-  
942 ent structures in ideal and resistive Hall MHD: The theory. *J. Geophys. Res.*,  
943 *114*. doi: 10.1029/2008JA013897
- 944 Torbert, R. B., Dors, I., Argall, M. R., Genestreti, K. J., Burch, J. L., Farrugia,  
945 C. J., ... Strangeway, R. J. (2020, February). A New Method of 3-D Magnetic  
946 Field Reconstruction. *Geophysical Research Letters*, *47*(3), e2019GL085542.  
947 (WOS:000529107400048) doi: 10.1029/2019GL085542

1 **Supporting Information for “Polynomial**  
2 **reconstruction of the magnetic field observed by**  
3 **multiple spacecraft with integrated velocity**  
4 **determination”**

Richard E. Denton<sup>1</sup>, Yi-Hsin Liu<sup>1</sup>, Hiroshi Hasegawa<sup>2</sup>, Roy B. Torbert<sup>3</sup>,

Wenya Li<sup>4</sup>, Stephen Fuselier<sup>5</sup>, and James L. Burch<sup>5</sup>

5 <sup>1</sup>Department of Physics and Astronomy, Dartmouth College, Hanover, New Hampshire, USA

6 <sup>2</sup>Institute of Space and Astronautical Science, JAXA, Sagami-hara, Japan.

7 <sup>3</sup>Institute for the Study of Earth, Oceans, and Space, University of New Hampshire, Durham, New Hampshire, USA.

8 <sup>4</sup>State Key Laboratory of Space Weather, National Space Science Center, Chinese Academy of Sciences, Beijing, China

9 <sup>5</sup>Space Science and Engineering Division Southwest Research Institute, San Antonio, Texas, USA.

10 **Contents of this file**

11 1. Text S1

12 2. Figures S1 to S5

13 **Additional Supporting Information (Files uploaded separately)**

14 1. Captions for Movies S1 to S7

15 Text S1 contains descriptions of the figures and movies.

16 **1. Text S1**

17 Figure S1 compares the reconstruction fields for case 1 to those of the simulation in the  $L$ - $N$  plane at the  $M$  value of the centroid of the virtual spacecraft. The format is

---

18 the same as that of Figure 6 in the paper, except for simulation reconstruction case 1.  
19 Similarly, Figures S2–S5 compare reconstruction fields to simulation fields for simulation  
20 reconstruction cases 7–10, respectively. Figure S3 is the same as Figure 6 in the paper,  
21 and Figure S5 is the same as Figure 7 in the paper; these are included here for easier  
22 comparison to the other figures.

23 Simulation reconstruction case 1 (Figure S1) uses the RQ-3D model with  $t_{\text{smooth}} =$   
24 0.4, whereas simulation reconstruction cases 7–10 (Figures S2–S5) show results for four  
25 different models (noted in the captions) for  $t_{\text{smooth}} = 0.8$ . All of Figures S2–S5 show  
26 reasonable agreement between the reconstruction and simulation fields, whereas there is  
27 a significant disagreement in Figure S1 (especially Figure S1e). This shows that use of a  
28 greater amount of smoothing significantly improves the reconstruction results.

29 Movie S1 shows the reconstruction fields for case 1 versus time in the  $L$ - $N$  and  $M$ -  
30  $N$  planes for case 1. Similarly, Movies S2–S5 show reconstruction fields for simulation  
31 reconstruction cases 7–10, respectively. The movies show the reconstruction field in the  
32  $L$ - $N$  plane, similar to that shown in the top panels of Figures S1–S5. The movies also  
33 show the reconstruction field in the  $M$ - $N$  plane.

34 In principle, if the  $M$  dependence is small, there should not be any variation of the field  
35 in the  $M$  direction. But there may appear to be significant variation in the  $M$  direction in  
36 the movies if the  $B_M$  and  $B_N$  components of the magnetic field are small (like at  $t = -0.3$ ;  
37 see top and bottom right panels of Movies S1–S5 at that time). There is usually less of  
38 this kind of problem for the magnetic field shown in the  $L$ - $N$  plane because  $B_L$  is usually  
39 the largest component of  $\mathbf{B}$ .

40 Again, Movies S2–S5, for cases 7–10, respectively, using  $t_{\text{smooth}} = 0.8$ , show more accu-  
41 rate reconstructions than Movie S1 for case 1, using  $t_{\text{smooth}} = 0.4$ .

42 Movies S6 and S7 have the same format as Movie S1, but Movie S6 shows the recon-  
43 struction fields for the 27 August 2018 MMS magnetotail reconnection event of section 4.1  
44 in the paper, and Movie S7 shows the reconstruction field for the 7 December 2016 MMS  
45 current sheet crossing event of section 4.2 in the paper.

46 **Movie S1.** Movie of the reconstruction fields versus time for simulation reconstruction  
47 case 1. The top panel shows the magnetic field averaged over the virtual spacecraft versus  
48 time. The current time of the movie frame is indicated by the vertical black line. The  
49 bottom left panel shows the reconstruction magnetic field in the  $L$ - $N$  plane. The black  
50 curves are streamlines of the magnetic field in the  $L$ - $N$  plane at the  $M$  value of the centroid  
51 of the virtual spacecraft. The color scale shows  $B_M$ , which is into the plane of the picture.  
52 The bottom right panel is similar, but showing the magnetic field in the  $M$ - $N$  plane.

53 **Movie S2.** Movie of the reconstruction fields versus time for simulation reconstruction  
54 case 7, using the same format as Movie S1.

55 **Movie S3.** Movie of the reconstruction fields versus time for simulation reconstruction  
56 case 8 (equivalent to case 2), using the same format as Movie S1.

57 **Movie S4.** Movie of the reconstruction fields versus time for simulation reconstruction  
58 case 9, using the same format as Movie S1.

59 **Movie S5.** Movie of the reconstruction fields versus time for simulation reconstruction  
60 case 10, using the same format as Movie S1.

61 **Movie S6.** Movie of the reconstruction fields versus time for the 27 August 2018 MMS  
62 magnetotail reconnection event of section 4.1 in the paper, using the same format as  
63 Movie S1.

64 **Movie S7.** Movie of the reconstruction fields versus time for the 7 December 2016 MMS  
65 current sheet crossing event of section 4.2 in the paper, using the same format as Movie S1.

66 Unlike Figure 13 in the paper, the color scale shows  $B_M$  (like in the other movies) rather  
67 than  $B_L$ .

68 **Figure S1. (caption not printing in Latex)** Comparison of reconstruction and sim-  
69 ulation magnetic field for simulation reconstruction case 1 using the RQ-3D model with  
70  $t_{\text{smooth}} = 0.4$ . The fields are plotted in the  $L$ - $N$  plane at the  $M$  value of the centroid  
71 of the virtual spacecraft. (a) Magnetic field averaged over the four virtual spacecraft.  
72 (b-i) In each pair of vertically arranged panels, reconstructed (top, with time label) and  
73 simulation (bottom, labeled “simulation”) magnetic streamlines in the  $L$ - $N$  plane (black)  
74 and magnetic field into the plane of the page,  $B_M$  (color scale).

## References

- 75 Denton, R. E., Sonnerup, B. U. O., Hasegawa, H., Phan, T. D., Russell, C. T., Strange-  
76 way, R. J., . . . Torbert, R. B. (2016). Motion of the MMS spacecraft relative to the  
77 magnetic reconnection structure observed on 16 October 2015 at 1307 UT. *Geophys.*  
78 *Res. Lett.*, *43*(11), 5589–5596. doi: 10.1002/2016gl069214
- 79 Denton, R. E., Sonnerup, B. U. O., Russell, C. T., Hasegawa, H., Phan, T. D., Strange-  
80 way, R. J., . . . Vines, S. K. (2018). Determining L-M-N Current Sheet Coordinates at  
81 the Magnetopause From Magnetospheric Multiscale Data. *J. Geophys. Res.*, *123*(3),  
82 2274–2295. doi: 10.1002/2017ja024619
- 83 Denton, R. E., Torbert, R. B., Hasegawa, H., Dors, I., Genestreti, K. J., Argall, M. R., . . .  
84 Fischer, D. (2020, February). Polynomial reconstruction of the reconnection magnetic  
85 field observed by multiple spacecraft. *JOURNAL OF GEOPHYSICAL RESEARCH-*  
86 *SPACE PHYSICS*, *125*(2). (tex.article-number: e2019JA027481 tex.eissn: 2169-  
87 9402 tex.orcid-numbers: Hasegawa, Hiroshi/0000-0002-1172-021X tex.researcherid-  
88 numbers: MMS, Science Team NASA/J-5393-2013 Hasegawa, Hiroshi/A-1192-2007  
89 tex.unique-id: ISI:000535395800016) doi: 10.1029/2019JA027481
- 90 Denton, R. E., Torbert, R. B., Hasegawa, H., Manuzzo, R., Belmont, G., Rezeau, L.,  
91 . . . Giles, B. L. (2021). Two-dimensional velocity of the magnetic structure ob-  
92 served on 11 <span class="nocase">July 2017 by the Magnetospheric Multiscale  
93 spacecraft</span>. *Journal of Geophysical Research-Space Physics*, *126*. doi:  
94 10.1029/2020JA028705
- 95 Fu, H. S., Cao, J. B., Vaivads, A., Khotyaintsev, Y. V., Andre, M., Dunlop, M., . . . Eriks-  
96 son, E. (2016, February). Identifying magnetic reconnection events using the FOTE

method. *JOURNAL OF GEOPHYSICAL RESEARCH-SPACE PHYSICS*, 121(2),  
 1263–1272. (tex.eissn: 2169-9402 tex.orcid-numbers: Khotyaintsev, Yuri/0000-0001-  
 5550-3113 Fu, Huishan/0000-0002-4701-7219 Vaivads, Andris/0000-0003-1654-841X  
 Liu, Wenlong/0000-0001-7991-5067 dunlop, malcolm w/0000-0002-8195-5137 Liu,  
 Wenlong/0000-0001-7991-5067 tex.researcherid-numbers: Khotyaintsev, Yuri/AAX-  
 9720-2021 Fu, Huishan/E-1507-2012 Vaivads, Andris/H-8169-2013 Liu, Wenlong/Y-  
 7669-2019 dunlop, malcolm w/F-1347-2010 Liu, Wenlong/G-5585-2013 tex.unique-id:  
 WOS:000373002100023) doi: 10.1002/2015JA021701

Fu, H. S., Vaivads, A., Khotyaintsev, Y. V., Olshevsky, V., Andre, M., Cao, J. B., ...  
 Lapenta, G. (2015, May). How to find magnetic nulls and reconstruct field topology  
 with MMS data? *JOURNAL OF GEOPHYSICAL RESEARCH-SPACE PHYSICS*,  
 120(5), 3758–3782. (tex.eissn: 2169-9402 tex.orcid-numbers: Fu, Huishan/0000-  
 0002-4701-7219 Khotyaintsev, Yuri/0000-0001-5550-3113 Vaivads, Andris/0000-  
 0003-1654-841X Retino, Alessandro/0000-0001-5824-2852 Lapenta, Giovanni/0000-  
 0002-3123-4024 tex.researcherid-numbers: Fu, Huishan/E-1507-2012 Khotyaintsev,  
 Yuri/AAX-9720-2021 Vaivads, Andris/H-8169-2013 Lapenta, Giovanni/J-5221-2016  
 tex.unique-id: WOS:000357869600035) doi: 10.1002/2015JA021082

Fu, H. S., Wang, Z., Zong, Q., Chen, X. H., He, J. S., Vaivads, A., & Olshevsky,  
 V. (2020). Methods for finding magnetic nulls and reconstructing field topology:  
 A review. In Zong, Q and Escoubet, P and Sibeck, D and Le, G and Zhang,  
 H (Ed.), *DAYSIDE MAGNETOSPHERE INTERACTIONS* (Vol. 248, pp. 153–  
 172). (ISSN: 0065-8448 tex.orcid-numbers: Fu, Huishan/0000-0002-4701-7219 Zong,  
 Qiugang/0000-0002-6414-3794 tex.researcherid-numbers: Fu, Huishan/E-1507-2012

- 120 Zong, Qiugang/L-1920-2018 tex.unique-id: WOS:000637603000010)
- 121 Fuselier, S. A., Trattner, K. J., Petrinec, S. M., Pritchard, K. R., Burch, J. L., Cassak,  
122 P. A., ... Strangeway, R. J. (2019, November). Stationarity of the reconnection  
123 x-line at earth's magnetopause for southward IMF. *JOURNAL OF GEOPHYS-*  
124 *ICAL RESEARCH-SPACE PHYSICS*, 124(11), 8524–8534. (tex.earlyaccessdate:  
125 NOV 2019 tex.eissn: 2169-9402 tex.orcid-numbers: Giles, Barbara L/0000-0001-  
126 8054-825X Strangeway, Robert/0000-0001-9839-1828 Fuselier, Stephen/0000-0003-  
127 4101-7901 Burch, James/0000-0003-0452-8403 Pritchard, Kristina/0000-0002-6523-  
128 6263 TRATTNER, KARLHEINZ/0000-0001-5169-109X tex.researcherid-numbers:  
129 Giles, Barbara L/J-7393-2017 tex.unique-id: WOS:000494920500001) doi: 10.1029/  
130 2019JA027143
- 131 Gershman, D. J., Avanov, L. A., Boardsen, S. A., Dorelli, J. C., Gliese, U., Barrie, A. C.,  
132 ... Pollock, C. J. (2017, November). Spacecraft and instrument photoelectrons  
133 measured by the dual electron spectrometers on MMS. *JOURNAL OF GEOPHYS-*  
134 *ICAL RESEARCH-SPACE PHYSICS*, 122(11), 11548–11558. (tex.eissn: 2169-9402  
135 tex.orcid-numbers: Giles, Barbara L/0000-0001-8054-825X Avanov, Levon/0000-  
136 0003-2357-4851 tex.researcherid-numbers: Giles, Barbara L/J-7393-2017 tex.unique-  
137 id: WOS:000419938600040) doi: 10.1002/2017JA024518
- 138 Haaland, S., Runov, A., Artemyev, A., & Angelopoulos, V. (2019, May). Char-  
139 acteristics of the flank magnetopause: THEMIS observations. *JOURNAL OF*  
140 *GEOPHYSICAL RESEARCH-SPACE PHYSICS*, 124(5), 3421–3435. (tex.eissn:  
141 2169-9402 tex.researcherid-numbers: Artemyev, Anton/AAO-8011-2020 tex.unique-  
142 id: WOS:000471601500019) doi: 10.1029/2019JA026459

- 143 Hasegawa, H., Denton, R. E., Nakamura, R., Genestreti, K. J., Nakamura, T. K. M.,  
144 Hwang, K. J., ... Saito, Y. (2019). Reconstruction of the Electron Diffusion Region of  
145 Magnetotail Reconnection seen by the MMS Spacecraft on 11 July 2017. *J. Geophys.*  
146 *Res.*, *124*(1), 122–138. doi: 10.1029/2018ja026051
- 147 Korovinskiy, D. B., Kiehas, S. A., Panov, E. V., Semenov, V. S., Erkaev, N. V., Divin,  
148 A. V., & Kubyshkin, I. V. (2021, May). The Inertia-Based Model for Reconstruction  
149 of the Electron Diffusion Region. *Journal of Geophysical Research-Space Physics*,  
150 *126*(5), e2020JA029045. (WOS:000657463000045) doi: 10.1029/2020JA029045
- 151 Li, W.-Y., Khotyaintsev, Y., V, Tang, B.-B., Graham, D. B., Norgren, C., Vaivads, A.,  
152 ... Wang, C. (2021, August). Upper-hybrid waves driven by meandering electrons  
153 around magnetic reconnection x line. *GEOPHYSICAL RESEARCH LETTERS*,  
154 *48*(16). (tex.article-number: e2021GL093164 tex.eissn: 1944-8007 tex.orcid-numbers:  
155 Khotyaintsev, Yuri/0000-0001-5550-3113 Lindqvist, Per-Arne/0000-0001-5617-9765  
156 Norgren, Cecilia/0000-0002-6561-2337 Dokgo, Kyunghwan/0000-0003-3917-7885  
157 Tang, BINBIN/0000-0002-9244-1828 Graham, Daniel/0000-0002-1046-746X An-  
158 dre, Mats/0000-0003-3725-4920 tex.researcherid-numbers: Khotyaintsev, Yuri/AAX-  
159 9720-2021 Lindqvist, Per-Arne/G-1221-2016 tex.unique-id: WOS:000688759800030)  
160 doi: 10.1029/2021GL093164
- 161 Liu, Y.-H., Li, T. C., Hesse, M., Sun, W. J., Liu, J., Burch, J., ... Huang, K.  
162 (2019, April). Three-dimensional magnetic reconnection with a spatially con-  
163 fined x-line extent: Implications for dipolarizing flux bundles and the dawn-  
164 dusk asymmetry. *JOURNAL OF GEOPHYSICAL RESEARCH-SPACE PHYSICS*,  
165 *124*(4), 2819–2830. (tex.eissn: 2169-9402 tex.orcid-numbers: Sun, Wei-Jie/0000-

- 166 0001-5260-658X Li, Tak Chu/0000-0002-6367-1886 Liu, Jiang/0000-0002-7489-9384  
167 Burch, James/0000-0003-0452-8403 tex.researcherid-numbers: Sun, Wei-Jie/E-8097-  
168 2012 Liu, Jiang/B-3015-2014 tex.unique-id: ISI:000477707800034) doi: 10.1029/  
169 2019JA026539
- 170 Manuzzo, R., Belmont, G., Rezeau, L., Califano, F., & Denton, R. E. (2019, December).  
171 Crossing of Plasma Structures by Spacecraft: A Path Calculator. *JOURNAL OF*  
172 *GEOPHYSICAL RESEARCH-SPACE PHYSICS*, *124*(12), 10119–10140. doi: 10  
173 .1029/2019JA026632
- 174 Shi, Q. Q., Pu, Z. Y., Zhang, H., Fu, S. Y., Xiao, C. J., Zong, Q. G., . . . Liu, Z. X. (2005).  
175 Simulation studies of high-latitude magnetospheric boundary dynamics. *Surveys in*  
176 *Geophysics*, *26*(1-3), 369–386. doi: 10.1007/s10712-005-1900-6
- 177 Shi, Q. Q., Shen, C., Dunlop, M. W., Pu, Z. Y., Zong, Q. G., Liu, Z. X., . . . Balogh,  
178 A. (2006). Motion of observed structures calculated from multi-point magnetic field  
179 measurements: Application to Cluster. *Geophys. Res. Lett.*, *33*(8). doi: 10.1029/  
180 2005gl025073
- 181 Shi, Q. Q., Tian, A. M., Bai, S. C., Hasegawa, H., Degeling, A. W., Pu, Z. Y., . . .  
182 Liu, Z. Q. (2019). Dimensionality, Coordinate System and Reference Frame for  
183 Analysis of In-Situ Space Plasma and Field Data. *Space Science Reviews*, *215*(4).  
184 doi: 10.1007/s11214-019-0601-2
- 185 Sonnerup, B. U. O., Hasegawa, H., Teh, W. L., & Hau, L. N. (2006). Grad-Shafranov re-  
186 construction: An overview. *J. Geophys. Res.*, *111*(A9). doi: 10.1029/2006JA011717
- 187 Sonnerup, B. U. O., & Teh, W.-L. (2008). Reconstruction of two-dimensional coherent  
188 MHD structures in a space plasma: The theory. *J. Geophys. Res.*, *113*(A5). doi:

189 10.1029/2007ja012718

190 Sonnerup, B. U. O., & Teh, W. L. (2009). Reconstruction of two-dimensional coherent

191 structures in ideal and resistive Hall MHD: The theory. *J. Geophys. Res.*, *114*. doi:

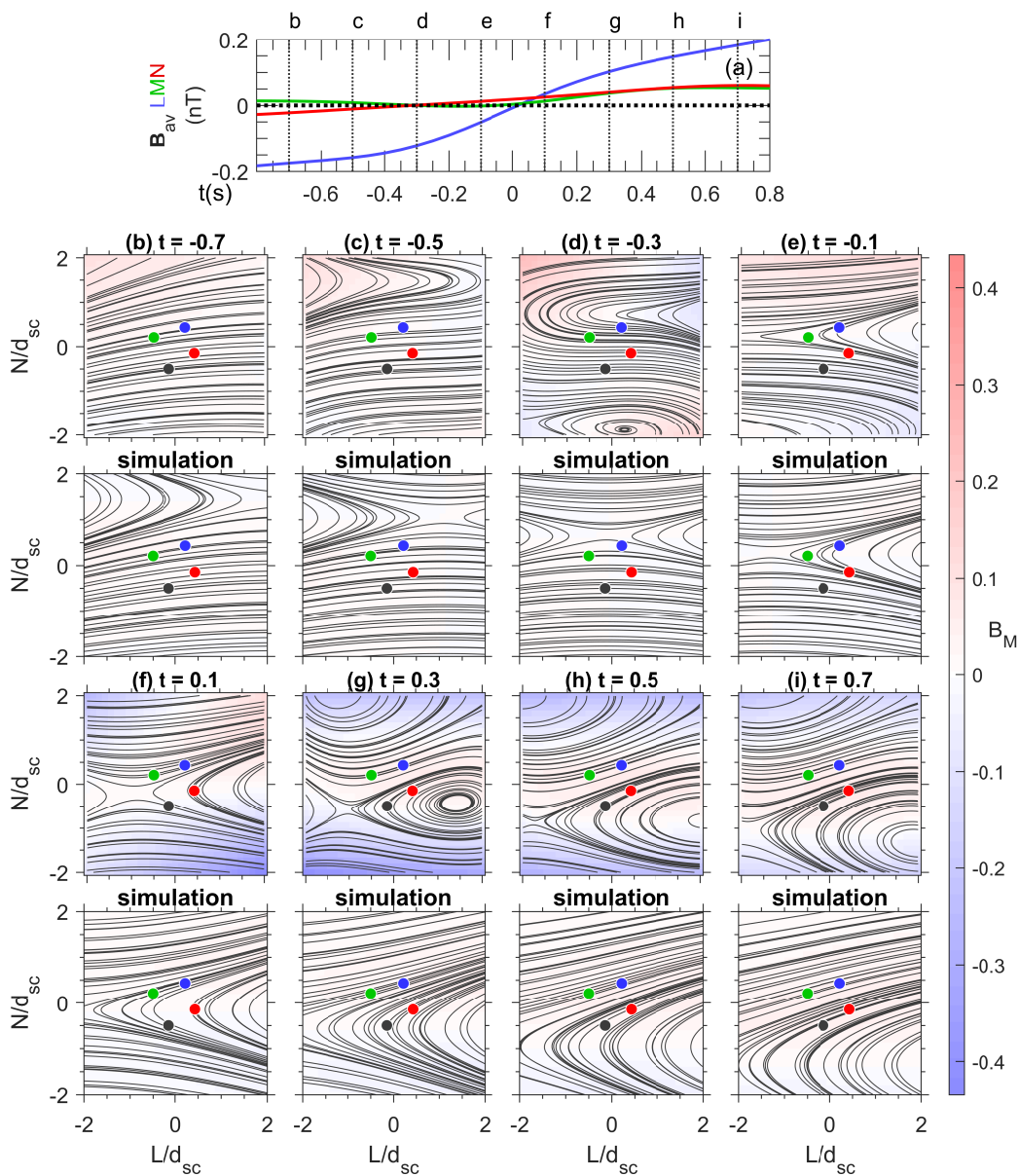
192 10.1029/2008JA013897

193 Torbert, R. B., Dors, I., Argall, M. R., Genestreti, K. J., Burch, J. L., Farrugia,

194 C. J., ... Strangeway, R. J. (2020, February). A New Method of 3-D Mag-

195 netic Field Reconstruction. *Geophysical Research Letters*, *47*(3), e2019GL085542.

196 (WOS:000529107400048) doi: 10.1029/2019GL085542



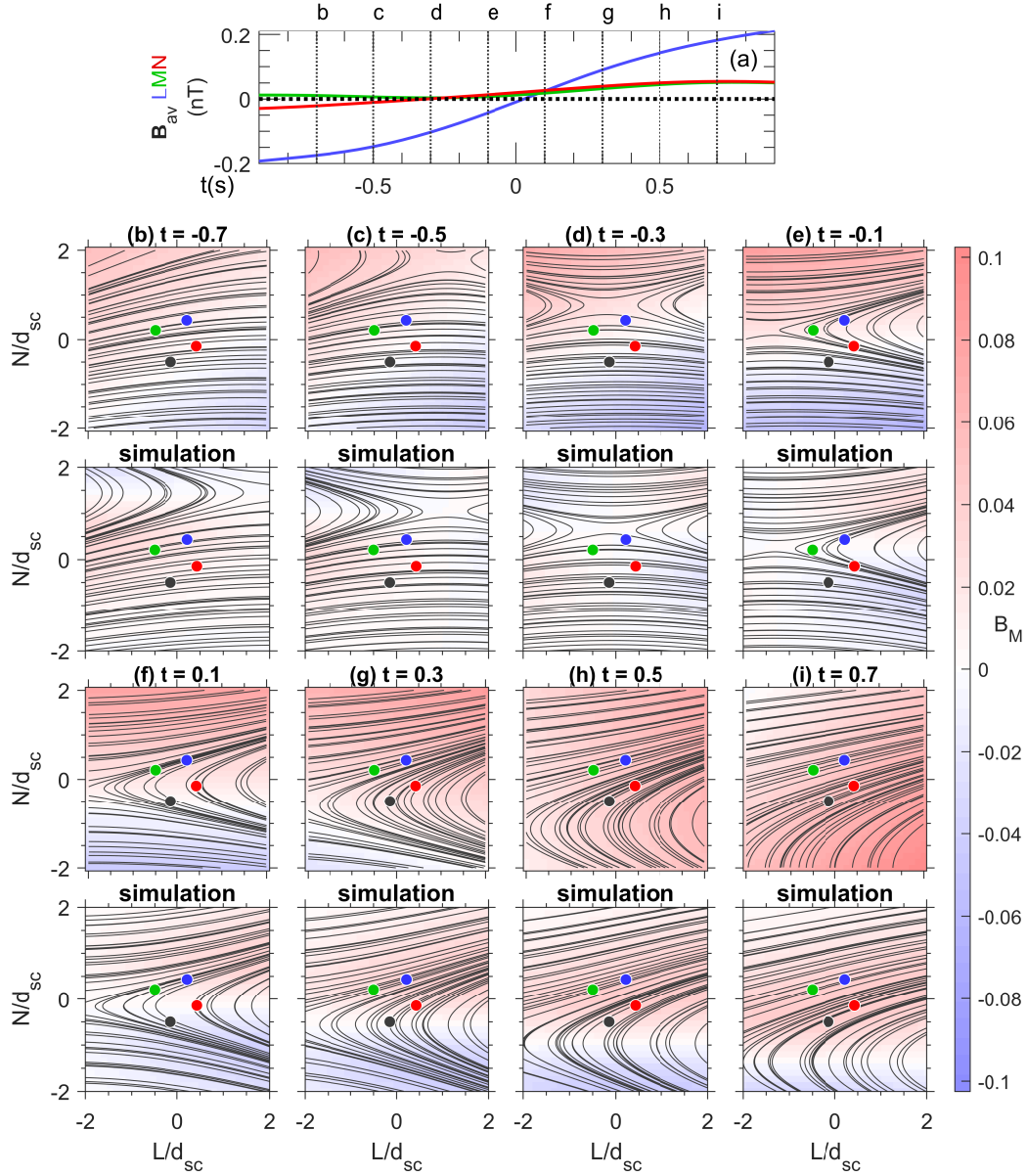


**Figure S2.** Comparison of reconstruction and simulation magnetic field in the  $L$ - $N$  plane for reconstruction case 7 using the LB-3D model with  $t_{\text{smooth}} = 0.8$ . The format is the same as that of Figure S1.

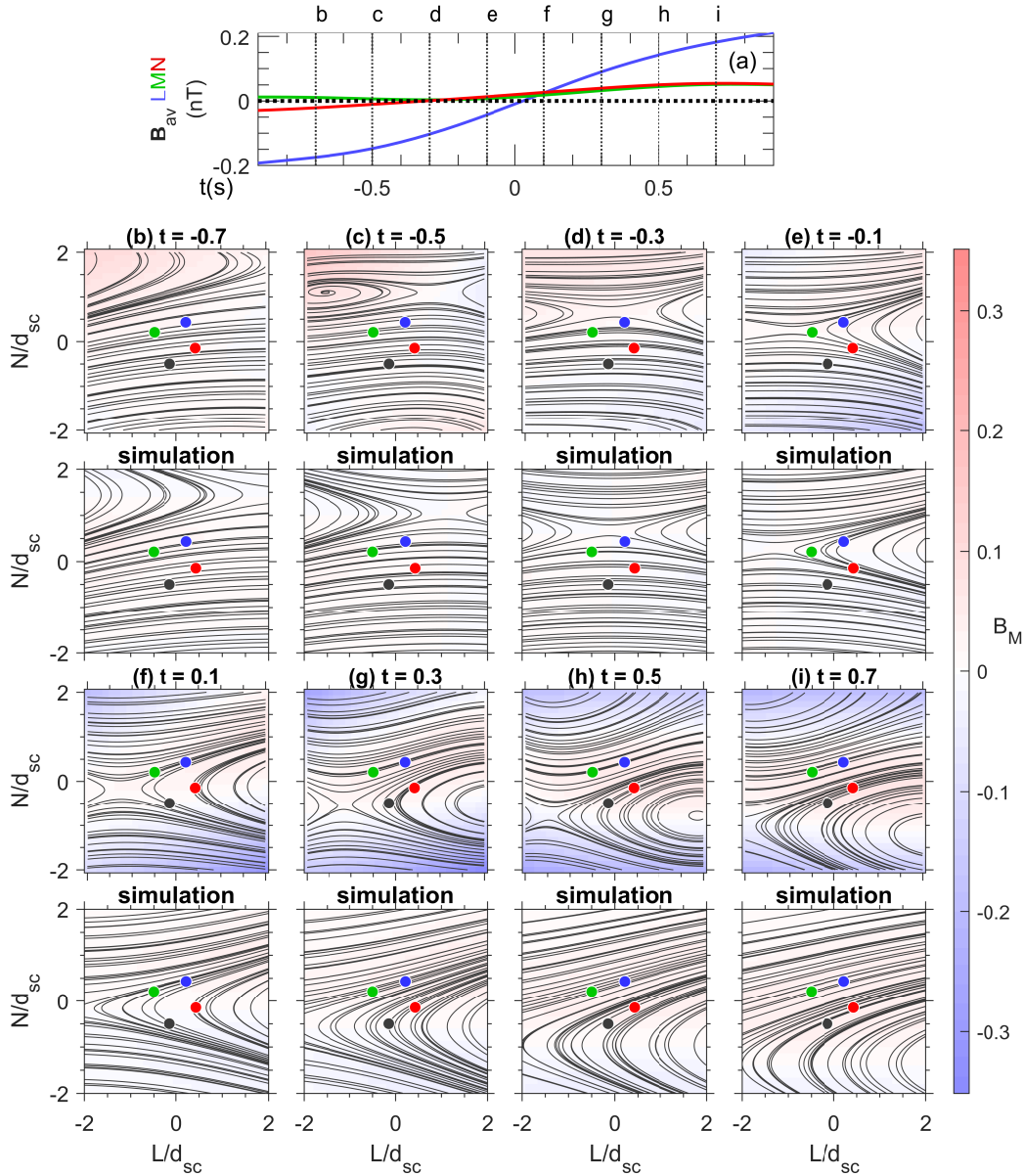


**Figure S3.** Comparison of reconstruction and simulation magnetic field in the  $L$ - $N$  plane for reconstruction case 8 (equivalent to case 2) using the RQ-3D model with  $t_{smooth} = 0.8$ . The format is the same as that of Figure S1.

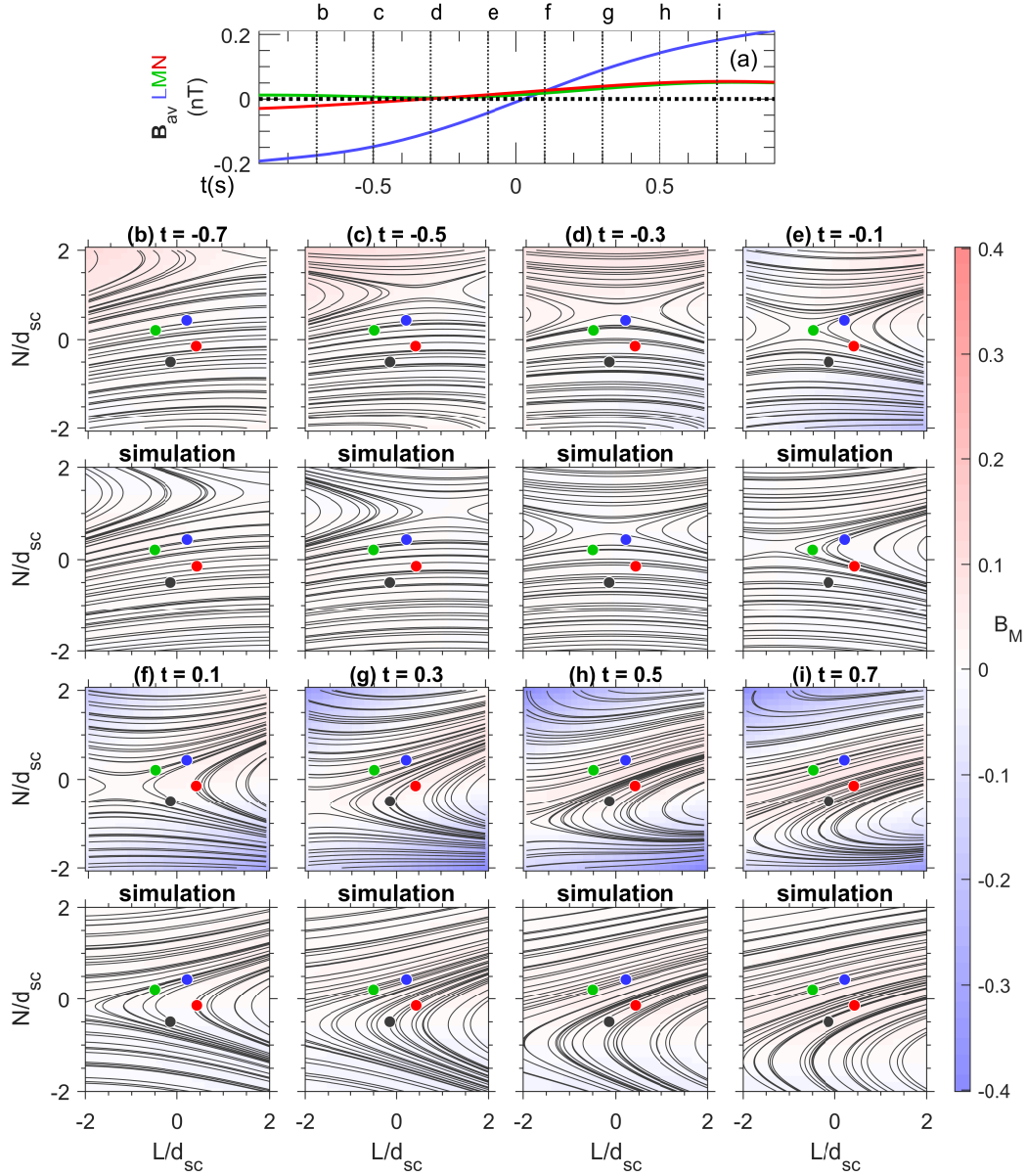


**Figure S4.** Comparison of reconstruction and simulation magnetic field in the  $L$ - $N$  plane for reconstruction case 9 using the Q-3D model with  $t_{smooth} = 0.8$ . The format is the same as that of Figure S1.

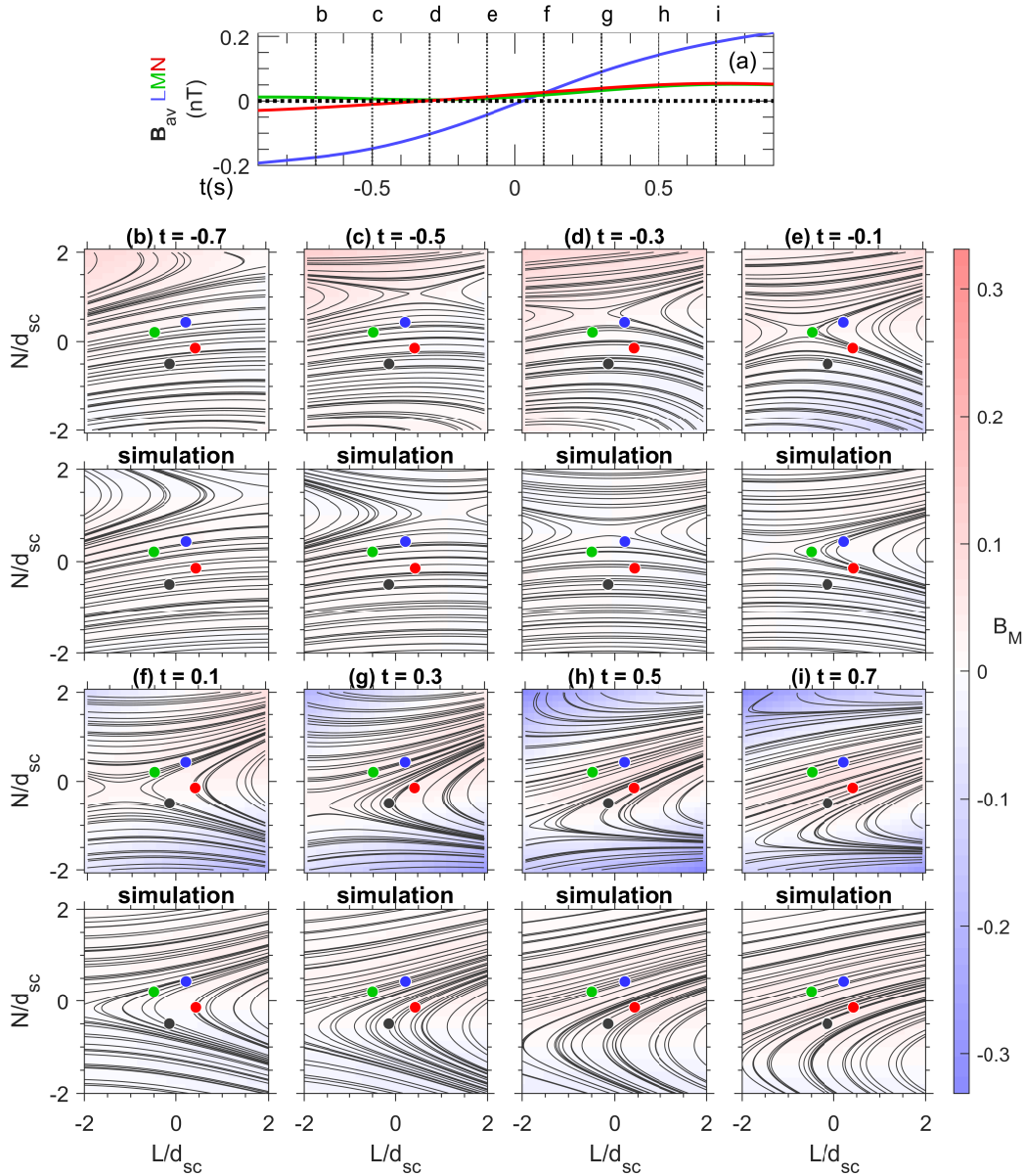


**Figure S5.** Comparison of reconstruction and simulation magnetic field in the  $L$ - $N$  plane for reconstruction case 10 using the CQ-3D model with  $t_{smooth} = 0.8$ . The format is the same as that of Figure S1. March 30, 2022, 4:11pm